

AD_____

GRANT NUMBER DAMD17-94-J-4055

TITLE: Direct Digital Mammography Using Capillary Optics

PRINCIPAL INVESTIGATOR: Carolyn A. MacDonald, Ph.D.

CONTRACTING ORGANIZATION: New York State University at Albany
Albany, New York 12222

REPORT DATE: September 1997

TYPE OF REPORT: Annual

PREPARED FOR: Commander
U.S. Army Medical Research and Materiel Command
Fort Detrick, Frederick, Maryland 21702-5012

DISTRIBUTION STATEMENT: Approved for public release;
distribution unlimited

The views, opinions and/or findings contained in this report are those of the author(s) and should not be construed as an official Department of the Army position, policy or decision unless so designated by other documentation.

DTIC QUALITY INSPECTED 2

REPORT DOCUMENTATION PAGE

Form Approved
OMB No. 0704-0188

Public reporting burden for this collection of information is estimated to average 1 hour per response, including the time for reviewing instructions, searching existing data sources, gathering and maintaining the data needed, and completing and reviewing the collection of information. Send comments regarding this burden estimate or any other aspect of this collection of information, including suggestions for reducing this burden, to Washington Headquarters Services, Directorate for Information Operations and Reports, 1215 Jefferson Davis Highway, Suite 1204, Arlington, VA 22202-4302, and to the Office of Management and Budget, Paperwork Reduction Project (0704-0188), Washington, DC 20503.

1. AGENCY USE ONLY (Leave blank)		2. REPORT DATE September 1997		3. REPORT TYPE AND DATES COVERED Annual (1 Sep 96 - 31 Aug 97)	
4. TITLE AND SUBTITLE Direct Digital Mammography Using Capillary Optics				5. FUNDING NUMBERS DAMD17-94-J-4055	
6. AUTHOR(S) Carolyn A. MacDonald, Ph.D.					
7. PERFORMING ORGANIZATION NAME(S) AND ADDRESS(ES) New York State University at Albany Albany, New York 12222				8. PERFORMING ORGANIZATION REPORT NUMBER	
9. SPONSORING/MONITORING AGENCY NAME(S) AND ADDRESS(ES) Commander U.S. Army Medical Research and Materiel Command Fort Detrick, MD 21702-5012				10. SPONSORING/MONITORING AGENCY REPORT NUMBER	
11. SUPPLEMENTARY NOTES					
19980310 029					
12a. DISTRIBUTION / AVAILABILITY STATEMENT Approved for public release; distribution unlimited				12b. DISTRIBUTION CODE	
13. ABSTRACT (Maximum 200) The overall objective of this proposal is to develop a mammographic system with extremely high scatter rejection and dynamic range, good resolution and low patient dose. This will be accomplished by developing a direct x-ray detector interfaced with a capillary x-ray optic. Capillary x-ray optics, invented in the mid-eighties, provide an innovative new way to control x-ray beams. A number of promising geometries are being studied: collimating optics with long and short focal lengths, with and without antiscatter optics, monolithic linear magnifying tapers, and monolithic focusing, demagnifying optics. The collimating optics have transmissions in excess of 30% at their design energies, with collection angles ranging from 8 to 12 degrees. Scatter rejection is very high from all the optics. The linear tapers resulted in nearly ideal contrast enhancements and simultaneously increase in MTF at all spatial frequencies. The rapidly growing modeling capability is already leading to improvements in the manufacturing processes. Direct digital detectors owe their high efficiency and resolution to the direct detection of x-ray photons without requiring phosphors for the conversion to visible light. One dimensional "imaging" was demonstrated with the CZT linear array. CID two dimensional array technology with small pixel sizes is another promising new technology for mammography.					
14. SUBJECT TERMS Mammography, Digital Mammography, Early Detection, Capillary X-Ray Optics, Breast Cancer				15. NUMBER OF PAGES 39	
				16. PRICE CODE	
17. SECURITY CLASSIFICATION OF REPORT Unclassified	18. SECURITY CLASSIFICATION OF THIS PAGE Unclassified	19. SECURITY CLASSIFICATION OF ABSTRACT Unclassified	20. LIMITATION OF ABSTRACT Unlimited		

FOREWORD

Opinions, interpretations, conclusions and recommendations are those of the author and are not necessarily endorsed by the U.S. Army.

✓ Where copyrighted material is quoted, permission has been obtained to use such material.

✓ Where material from documents designated for limited distribution is quoted, permission has been obtained to use the material.

✓ Citations of commercial organizations and trade names in this report do not constitute an official Department of Army endorsement or approval of the products or services of these organizations.

 In conducting research using animals, the investigator(s) adhered to the "Guide for the Care and Use of Laboratory Animals," prepared by the Committee on Care and Use of Laboratory Animals of the Institute of Laboratory Resources, National Research Council (NIH Publication No. 86-23, Revised 1985).

 For the protection of human subjects, the investigator(s) adhered to policies of applicable Federal Law 45 CFR 46.

 In conducting research utilizing recombinant DNA technology, the investigator(s) adhered to current guidelines promulgated by the National Institutes of Health.

 In the conduct of research utilizing recombinant DNA, the investigator(s) adhered to the NIH Guidelines for Research Involving Recombinant DNA Molecules.

 In the conduct of research involving hazardous organisms, the investigator(s) adhered to the CDC-NIH Guide for Biosafety in Microbiological and Biomedical Laboratories.

Carolyn M. Donald 9/29/97
PI - Signature Date

Table of Contents

Table of Contents	4
Introduction.....	5
Nature of the Problem.....	5
Purpose.....	5
Background.....	6
Benefits of Digital Mammography.....	6
Capillary Optics	6
Digital X-ray Detection.....	7
Proposed Statement of Work: Status.....	8
Progress to Date	9
Polycapillary Optics	9
Single Fibers.....	9
Transmission.....	9
Absorption Measurement	14
Collimating Optics	15
8 keV Prototype.....	15
20 KeV prototype	19
Anti-Scatter Optics.....	20
Straight MultiFiber Optic.....	20
Magnifying Linear Monolithic Optics.....	21
Demagnifying, Focusing Monolithic Optics	30
Direct Digital Detectors.....	32
CZT Detector	32
CID Detector	36
Conclusions	37
References	38

Introduction

Nature of the Problem

While it is hoped that molecular detection and intervention will one day provide a more effective treatment modality, currently, in the words of the Report to the U.S. Army Medical Research and Development Command on the Strategies for Managing the Breast Cancer Research Program, "no dominant etiology for breast cancer has emerged...[this] would lessen the prospects for any quick and easy prevention strategies.... mammography is the method of choice for screening women to detect breast cancer ... mammography has proven to be the most effective means of reducing breast cancer morbidity and mortality."

The primary theoretical limitations of mammography are the system resolution, which determines the minimum size of the detectable malignancy, and the need to expose the patient to ionizing radiation. Using innovative new technology to improve system resolution and reduce required dose will increase the effectiveness of this proven screening modality, with a direct and immediate impact on mortality. In addition, this direct digital system can avail itself of the advantages of digital processing, including improved image contrast and resolution at reduced radiation dose.¹ In practice, mammographic imaging is often limited by quality assurance issues, which can also be favorably addressed by digital processing.

Purpose

The overall objective of this proposal is to develop a mammographic system with extremely high scatter rejection and dynamic range, good resolution and low patient dose. This will be accomplished by developing a direct x-ray detector interfaced with a capillary x-ray optic in an appropriately designed mammographic system.

Kumakhov capillary x-ray optics, invented in the mid-eighties, provide an innovative new way to control x-ray beams. Such optics will provide extremely efficient scatter rejection, while allowing beam magnification, demagnification, and shaping to match with the newly developing high efficiency direct x-ray detectors. These detectors owe their high efficiency and resolution to the direct detection of x-ray photons without requiring phosphors for the conversion to visible light. An integrated system of optics and detectors will be developed in a highly collaborative effort involving recognized leaders in the fields of capillary optics, x-ray detectors, digital radiology, and mammography. Testing will be performed on each of the elements independently, and as an integrated unit in a mammographic system.

Background

Benefits of Digital Mammography

Conventional film/screen mammography suffers from limited dynamic range and film granularity, which can reduce the sensitivity of detection of microcalcifications. Digital detection provides high dynamic range, improving contrast, and greatly increasing the tolerance of the final image to under- or over-exposure. Digital images can be enhanced and are amenable to computer aided diagnosis. Spectral information can be included if it is available. Finally, digital images can be quickly transported for skilled consultation.

Capillary Optics

Kumakhov capillary optics are bundles of hollow glass capillary tubes with inner diameters as small as a few microns. A typical fiber is shown in Figure 1. X rays incident on the interior of the glass tubes at small angles can be guided down the tubes by total external reflection.

The polycapillary fibers guide x rays in a manner analogous to the way fiber optics guide light. Arrays of curved tapered fibers can be used to focus, collimate and filter x-ray radiation.^{2,3,4,5,6} Such arrays can be manufactured by stringing hollow glass polycapillaries through metal grids, as shown in Figure 16, or manufactured without grids as a monolithic optic, as shown in Figure 2.

The critical angle for total external reflection of x rays by glass polycapillaries is

$$\theta_c = \frac{\omega_p}{\omega}, \quad (1)$$

where ω_p is the plasma frequency of the glass, about 30 eV, and ω is the photon frequency. The critical angle is 1.5 milliradians at 20 keV. The x rays can be transmitted in a curved tube so long as the tube is small enough and bent gently enough that the angles of incidence are kept less than the critical angle. For a given radius of curvature, this requires increasingly small diameter tubes as the x-ray energy is raised. In order to avoid the mechanical limitations of such small tube sizes, polycapillary fibers are employed with channel sizes (typically 1-30 μm) much smaller than the outer diameter (300-1000 μm).

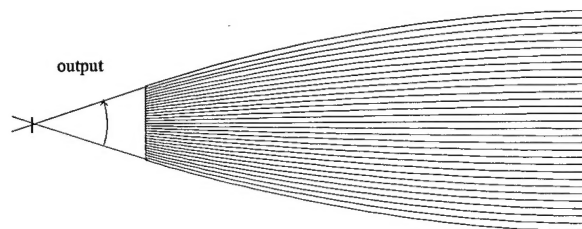


Figure 2. Monolithic optic geometry.

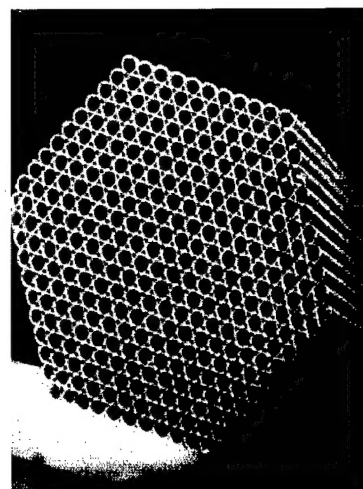


Figure 1. Cross sectional scanning electron micrograph of polycapillary fiber 0.5 mm in diameter.

The use of Kumakhov capillary optics in place of more conventional scatter reduction grids in a mammographic system has significant potential to provide improved resolution, increased contrast enhancement, and reduced dose in mammographic imaging. The optics can also be used to mate the radiographic image with a digital detector by appropriate

choice of magnification, demagnification, or separation to discrete chips. In addition, a pre-patient optic could be employed to increase the available intensity in a fan beam relative to simple slot collimation.

Digital X-ray Detection

In almost all radiological systems, detection of x rays is performed by the use of a "phosphor" screen which converts absorbed x rays into visible light photons. The visible light is then recorded on an analog medium, such as film, or detected by a digital detector. The phosphor screen is used because most detectors, including film, are not particularly sensitive to x rays. The use of a screen-film combination reduces radiation requirement compared to direct exposure film by a factor of 50-100.⁷ This increase in sensitivity occurs at the expense of resolution. The modulation transfer function of a good film-screen combination drops to less than 0.1 at a frequency of 15 lp/mm.⁷ The choice of screen thickness is a trade-off between detected quantum efficiency, which improves with increasing thickness, and resolution, which is degraded by light blur in a thick screen.⁸

Efficient direct x-ray detection virtually eliminates the tradeoff between spatial resolution and sensitivity because of the elimination of the phosphor screen. Direct x-ray detectors can provide resolution of 20 lp/mm or better with nearly 100% Detector Quantum Efficiency (DQE).

An especially promising direct x-ray detector is the cadmium zinc telluride (CZT) semiconductor detector recently developed by Digirad, formerly Aurora Technologies. The DQE of a .5 mm thick CZT detector is essentially unity at 20 keV, while the resolution is to first order independent of thickness. CZT detectors are similar in many respects to cadmium telluride (CdTe) detectors which have been available commercially for many years. The replacement of a fraction of the Cd with Zn causes a wider bandgap and results in a resistivity increase of two orders of magnitude. This high resistivity is an important factor because it reduces leakage current, a significant source of performance degrading noise. Leakage current noise generally limits the use of CdTe detectors by requiring longer integration times and larger pixel sizes.

Another promising direct digital detector is the Charge Injection Device (CID). Like the more common CCD (Charge couple device) CID technology allows for rapid array imaging. Unlike the CCD, the CID is very radiation resistant. Also unlike CCDs, for which the entire array must be read out and simultaneously cleared as a unit, CID pixels can be read individually, repeatedly, and nondestructively, leading to very high dynamic range. CID pixel well depths are also deeper than conventional CCDs, leading to a substantial reduction in blurring from high energy x-ray photons.

Proposed Statement of Work: Status

- I. Development of Capillary Optic Mammographic System: Months 1-36
 - I.A. Single Capillary Measurements: Months 1-6: Completed
 - I.B. Simulation of Design Strategies: Months 6-18: Completed
 - I.C. Assembly and Testing of Prototype Optic: Months 18-24: Completed
 - I.D. Design of Final Mammographic Optics and Detector Unit: Months 20-28: 90% Completed
 - I.E. Assembly and Testing of Final Optic: Months 28-36: Delayed, Ongoing
- II. Development of Digital Detector: Months 1-24
 - II.A. Fabricate CZT Linear Detector Arrays: Months 1-24: Completed
 - II.B. Develop Interconnect Methodology (Wire Bonding): Months 2-8: Completed
 - II.C. Assemble and Test Proof of Principle Detector/Multiplexer Hybrid : Months 2-12: Completed
 - II.D. Assemble Additional Hybrid Arrays: Months 12-24: Changed
- III. Mammographic Measurements: Months 18-48
 - III.A. Measurement of Prototype System: Months 18-36: Completed
 - III.A.1 Design and Fabrication of Test System: Months 18-24: Completed
 - III.A.2. Measure Primary Transmission in a Mammographic Geometry: Months 24-30: Completed
 - III.A.3 Measure Transmission of Scattered Radiation: Months 24-30: Completed
 - III.A.4. Spectral Measurements: Months 24-30: Completed
 - III.A.5. Investigate Artifacts due to Capillary Structure: Months 30-36: Ongoing
 - III.A. 6. Measure Contrast Improvement and Resolution: Months 30-36: Ongoing
 - III.B. Measurement of Final Optics/Detector System: Months 28-48
 - III.B.1. Design and Fabrication of Measurement System: Months 28-36: Completed
 - III.B.2. Measure Primary Transmission in a Mammographic Geometry: Months 36-42: Future
 - III.B.3. Measure Transmission of Scattered Radiation: Months 36-42: Future
 - III.B.4. Spectral Measurements: Months 36-42: Future
 - III.B.5. Investigate Artifacts due to Capillary Structure: Months 42-48: Future
 - III.B.6. Measure Contrast Improvement and Resolution: Months 42-48: Future
 - III.B.7. Evaluate Image Quality Using RMI Breast Phantom: Months 42-48: Future

Progress to Date

Rather than follow a step by step task listing, this progress report has been divided into subject areas to provide a more coherent description of the current state of the art. While there has been substantial manufacturing delays in the production of monolithic optics, the available optics have lent themselves to a thorough systematic review of the various optics geometries proposed for this project. Representative measurements have been made on a large number of optics geometries, rather than relying on the simple simulations initially proposed for this project. Manufacturing issues are discussed as well.

The proof-of-principle linear CZT array has been demonstrated, but an alternate detector path, CID technology appears equally promising. Studies of both detectors are discussed.

Polycapillary Optics

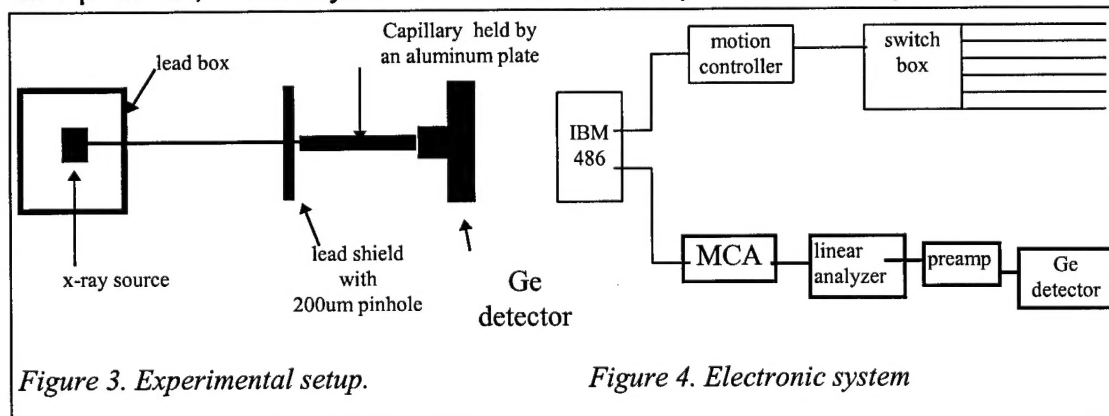
Measurements and simulations have been performed on several geometries: single fibers; multifiber collimating optics; multifiber straight antiscatter optics; and magnifying and demagnifying monolithic optics.

Single Fibers

TRANSMISSION

An important step in optics development was the breakthrough in modeling capacity, which has led to an unprecedented level of theoretical understanding of the basic properties of polycapillary fibers, especially fiber defects. To evaluate the experimental performance of polycapillary fibers, and design capillary optics, it is necessary to be able to predict theoretical behavior for complex geometries. The modeling program for single fibers is based on a Monte Carlo simulation of simple geometrical optics. The computational speed is greatly enhanced by a reduction to two dimensions by projecting the trajectory onto the local fiber cross-section.⁹ Reflectivities are computed from standard tables.¹⁰ Significant recent progress has been made in understanding the effect of capillary profile error, waviness and roughness on the transmission spectra.¹¹ This is extremely important in providing feedback to the manufacturing process.

The experimental arrangement for single capillary measurements is shown in Figure 3 and Figure 4. An optical rail affixed to an optical table carries an x-ray source, fiber platform, and x-ray detector. Each can be positioned independently in three



Type	Description	Outer Diameter, mm	Channel Size, μm	Area	Length mm
A	Borosilicate	0.5	12	65%	105
B	Lead glass	0.5	12	52%	95
C	Borosilicate	0.75	22	50%	136
D	Borosilicate	4	12	55%	130
E	Borosilicate	0.3	4-5	55%	105

Table 1. Description of polycapillary fibers

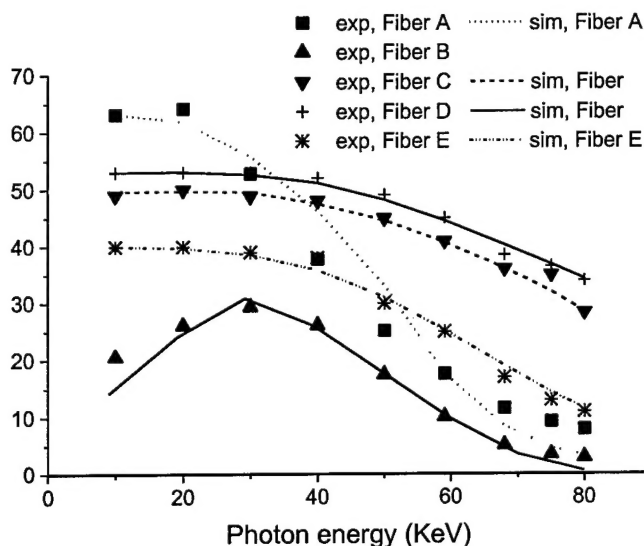


Figure 5. Measured transmission versus energy for polycapillary fibers listed in Table 1.

dimensions. A collimator is placed before the fiber and any remaining x-ray leakage around the fiber is eliminated with metal powder or filings. The measured fibers are described in Table 1.

The results of transmission studies as a function of photon energy are shown in Figure 5.^{12,13} All of the fibers except the lead glass have transmissions at 20 keV nearly equal to their fractional open area (the fraction of the cross section of the capillary which is open space, the rest being glass walls). This transmission corresponds to the primary transmission

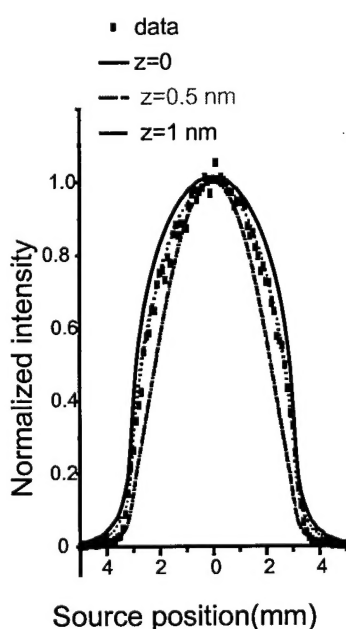


Figure 7. Source scans.

expected for a linear capillary optic employed as an antiscatter grid. The transmission falls off at higher energies. Modeling this transmission spectra has lead to a greater understanding of defects in polycapillary optics.

In Figure 7, simulations with or without roughness corrections are compared with the experimental data. In these measurements the source is scanned transverse to the fiber axis. The simulation with a roughness height of 0.5 nm fits the experimental data quite well. It is definitely over-corrected when the roughness is 1.0 nm. The same simulations, shown in Figure 6, are

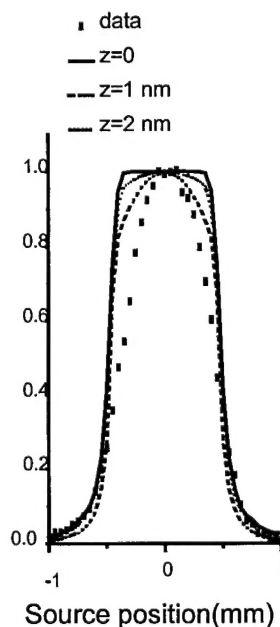


Figure 6. Source scans at 68 keV.

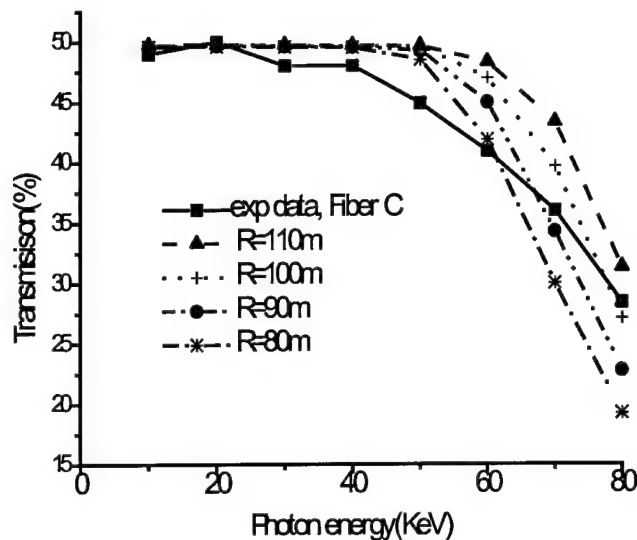


Figure 8. Transmission spectra of Fiber 3 simulated with different bending curvature alone and compared with experimental data

because of the small critical angle. A comparison between experimental data and simulations with different bending is shown in Figure 8. The figure shows that the simulations with bending alone do not fit the experimental data well, which indicates that bending is not the only factor which causes the high energy transmission to drop. However, from Figure 8, we can see that the range of the bending radius must be larger than 100m to give the observed transmission at the highest energy(80KeV).

Capillary surface oscillations with wavelengths shorter than the capillary length and longer than the wavelength of the roughness are called waviness. The detailed shape of waviness is unknown. Its average effect can be considered as a random tilt of the glass wall, so that the grazing angle of the photon is changed by a random amount, $\delta\theta$, after every bounce. $\delta\theta$ is a random number between $-\Delta\theta_{\max}$ and $\Delta\theta_{\max}$ if $\theta \geq \Delta\theta_{\max}$. The maximum random tilt angle $\Delta\theta_{\max}$ is an adjustable parameter which depends on the waviness of the polycapillary fiber. To keep θ' positive, $\delta\theta$ is taken to be a random number between $-\theta$ and $\Delta\theta_{\max}$ when $\theta < \Delta\theta_{\max}$. Since a photon with a incident angle smaller than $\Delta\theta_{\max}$ has a larger chance

also carried out at 68 keV, where the width of the curve is narrower than that at 10 keV because of the smaller critical angle. Photons also experience fewer bounces on average. Simulations with roughnesses as large as 1.0 and 2.0 nm still could not fit the data. Knowing that 1.0 or 2.0 nm roughness is definitely too large at 10 keV, we can determine that the roughness correction by itself is not sufficient at high energy to reproduce source scan measurements. Other effects need to be considered. These are bending and waviness.

A slight bending of the capillary can dramatically reduce the transmission of high energy photons

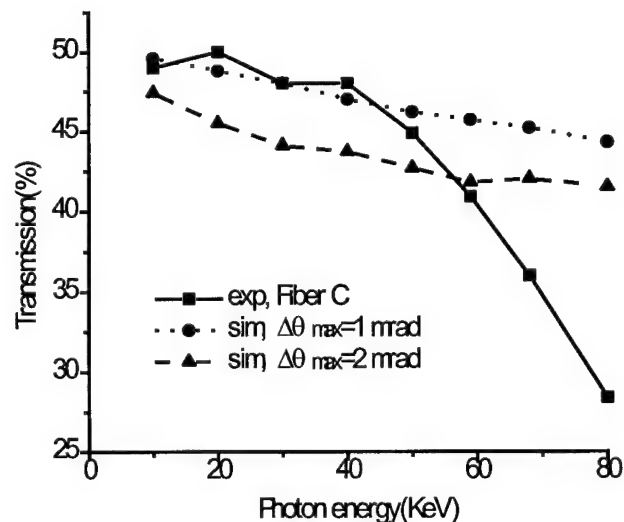


Figure 9. Simulations of transmission spectra with waviness only compared with the experimental data.

to experience an angle increase than an angle decrease, this is physically reasonable. In Figure 9, simulations with waviness corrections with $\Delta\theta_{\max}$ set at 1 mrad and 2 mrad, which is comparable to the critical angle, are compared with the experimental data. This figure shows that simulations with waviness alone do not fit the experimental data. This is because the waviness correction changes the reflected angle, not the profile. In fact the capillary is still considered to be straight, so those photons which have few reflections will not be significantly effected by waviness.

Finally the waviness and bending are combined by increasing the bending radius R , roughly determined in Figure 8, and adding a waviness parameter, $\Delta\theta_{\max}$.

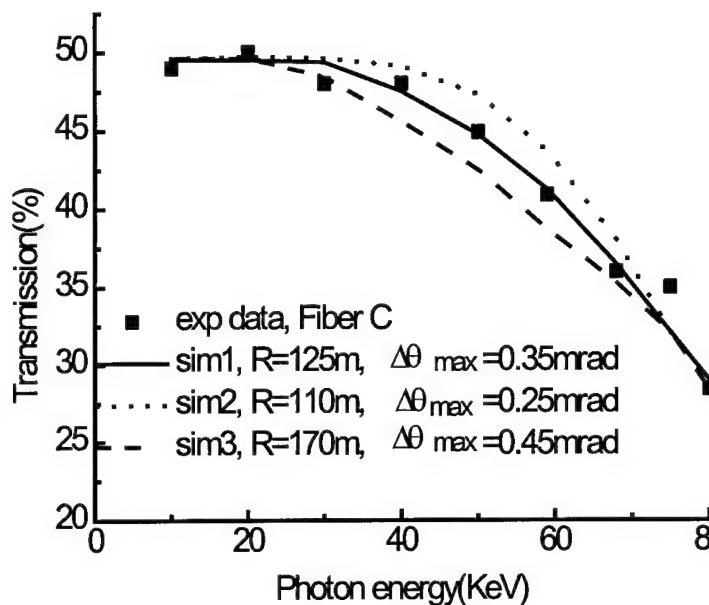


Figure 10. Simulated transmission spectra with different bending and waviness compared with the experimental data in search for the best fitting of Fiber C.

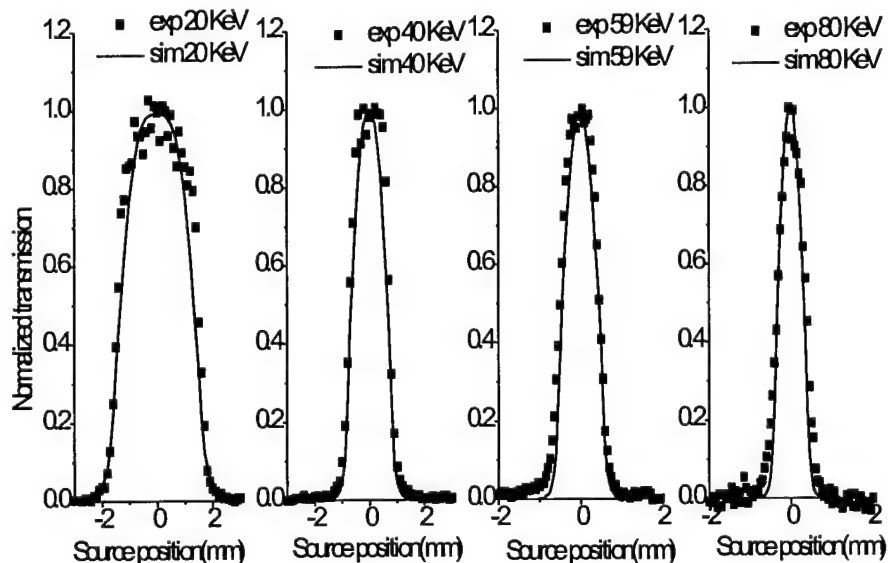


Figure 11. Simulated source scan curves compared with experimental data at four different photon energies. Parameters are: $R = 125$ m, $\Delta\theta_{\max} = 0.35$ mrad, roughness height = 0.5 nm.

Several trials are shown in Figure 10. Sim2 has too much bending and not enough waviness; sim3 has too much waviness and not enough bending; sim1 is the best fit. Roughness is also included in those simulations. The source scan simulation with the three fixed parameters are plotted along with the experimental data in Figure 9 for four more photon

TABLE 2. Simulation Fitting Parameters. Simulation 1-4 correspond to borosilicate fibers A,B,C, and E.

Simulation	Bending radius R (m)	Waviness $\Delta\theta$ (mrad)	Roughness height z (nm)
1	35	0.4	0.7
2	125	0.35	0.5
3	110	0.285	0.8
4	90	0.45	0.8

keV. This capillary is thin (500 μm in diameter) and flexible, and therefore difficult to keep straight in the measurement apparatus. Any slight bending is more significant at high energies, where the critical angles are smaller. Transmission for fiber C and fiber D are nearly flat up to 60 keV. As noted in table 1, these two fibers have larger outer diameters, so are more rigid and easier to keep straight. Even though these two fibers have lower fractional open area than fiber A, their transmissions exceed that of fiber A at energies above 30 keV. The simulation also requires smaller waviness and bending correction for these two fibers. Fiber E is thinner than type A, but its transmission is flat to 40 keV. The reason for this is that this fiber has small channel size which reduces the sensitivity to waviness and other profile errors. But the small channel size also results in more reflections being needed for a photon to traverse the fiber and may also have introduced other defects such as closed channels. This is why the transmission is

energies. They all fit quite well.

A similar procedure was used to determine the simulation parameters for the remaining fibers. The results are shown in Figure 5. The fitting parameters are shown in table 2. Examining Figure 5 again, the channel transmission for fiber A shows a rapid drop for energies above 30

only 40% under 40 keV although the open area is around 55%. The high transmissions and the simulation results show that the quality of the polycapillary fibers is quite good. The surface roughness is between 0.5 and 0.8 nm, and bending curvature is above 110 meters for fibers C and D. The lead glass fiber quality is somewhat poorer, with 0.8 nm roughness, 0.45 mrad waviness, 28 m curvature, and channel blockages equivalent to 50 μm of lead glass along the 9.5 cm of length.

Transmission was also measured of deliberately curved fibers, which can be used to deflect x-ray beams over larger angles. The results are shown

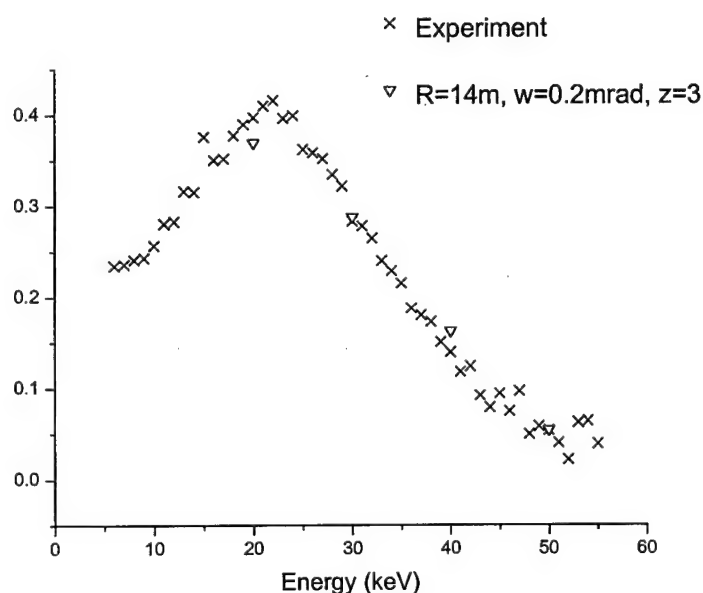


Figure 12. Transmission efficiency of 350 μm OD polycapillary fiber with 6 μm channel diameter. The fiber length is 25 cm. Simulated values are shown for 20, 30, 40, 50 keV x rays. The parameters are curvature, R; waviness, w; and roughness, z.

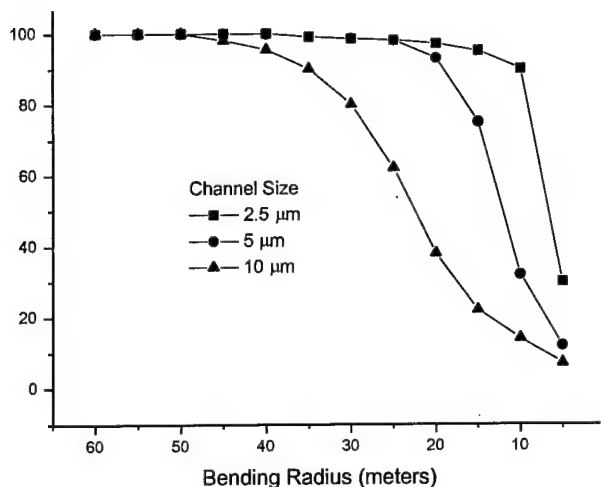


Figure 13. Simulated transmission as a function of bending radius at 50 keV, with no waviness or roughness.

angle which is larger than the critical angle.

The setup includes a source, a pinhole with size of 200 μm , an aluminum plate which is used to hold the capillary bundle, and a Germanium detector. The source has a maximum operate voltage of 100 kV. The source and aluminum plate are attached on linear stages which are controlled by linear actuators. Both the source and the optics fiber can move freely in two perpendicular directions transverse to the x-ray beam. An additional rotary stage is used to rotate the aluminum plate, so that the optic can also be rotated in horizontal direction.

The experiment starts with the alignment between the source, pinhole, and detector, by adjusting the source and fiber positions. After alignment, the optic was tilted to an angle larger than the largest critical angle for the measured energy range, then translated out of the x-ray beam. While the capillary optics were moved into the x-ray beam step by step, an x-ray spectrum was taken by the germanium detector after the optics at each step. The acquire time

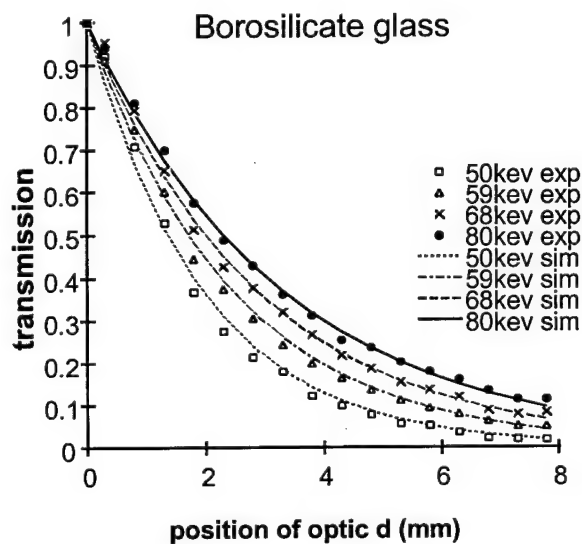


Figure 15. Absorption measurement

in Figure 12. Simulated transmission for a single fiber with various channel sizes is shown in Figure 13.

ABSORPTION MEASUREMENT

To achieve total scatter rejection, the glass wall of the optics must be thick enough to absorb the scattered x rays from various directions while allowing the majority of the primary x rays to pass. The absorption of the polycapillary fiber bundle was measured by tilting the optic to an

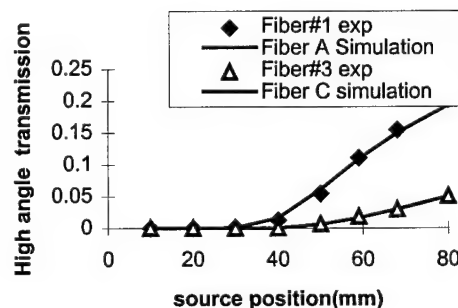


Figure 14. High angle transmission through capillary walls as a function of photon energy.

for each step was 30 seconds. The transmission at every step is the ratio between the counts without optics and the counts with optics at that step. Transmission at different energies as a function of optic position is plotted in Figure 15 along with the theoretically calculated values.

Large angle transmission can be calculated as

$$T_s = e^{-(1-f) \cdot \mu \cdot \rho \cdot x} \quad (2)$$

where μ is the mass attenuation of the material which can be calculated from tabulated values²¹ according to the mass composition, ρ is the density of the glass, f is the open area of the capillary bundle, and x is the distance that the x-ray beam travels across the fiber. x can be calculated from capillary movement d and capillary tilting angle,

$$x = d / \alpha, \quad (3)$$

where α is the tilting angle in rad. Theoretical calculated numbers from equation (2) are compared with the experimental result in Figure 15. The theoretical values fit well with the experimental data. Measured and theoretical transmission of a polycapillary fiber as a function of photon energy is shown in Figure 14. This "high angle transmission" corresponds to scatter transmission for the capillary optics used as an antiscatter grid, and is less than 1% at 20 keV. The solid line is a theoretical calculation, which agrees quite well with the data.

Collimating Optics

8 KEV PROTOTYPE

Because of the technological difficulties in producing large area monolithic optics, the fastest route to a large scale antiscatter system for contrast measurements is a straight optic. The low angular acceptance of the capillary channels requires that

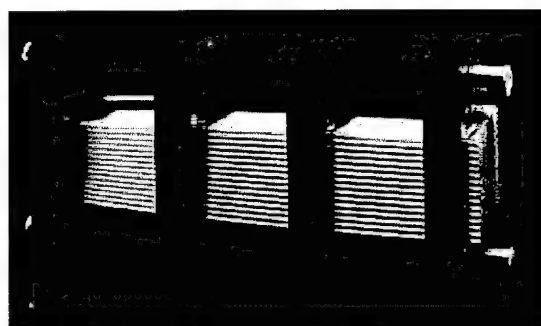


Figure 16. Multifiber collimating lens.

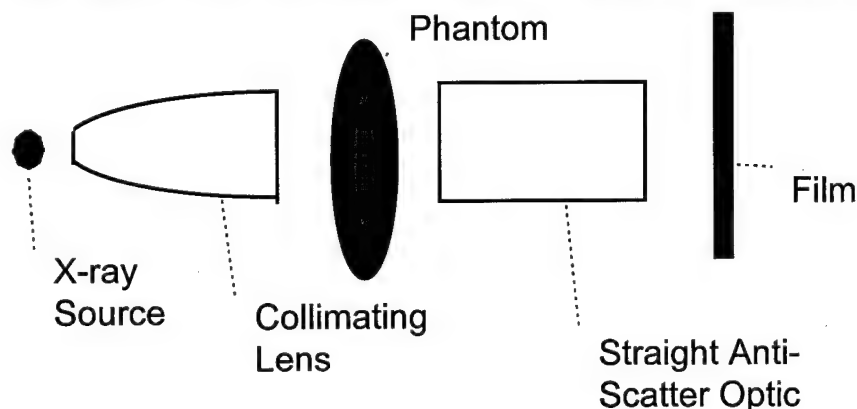


Figure 17. Set-up for Anti-scatter measurements.

such an optic be used with a collimated beam, as shown in Figure 17. A collimating lens, similar to that pictured in Figure 16, and a straight fiber bundle of 3 cm

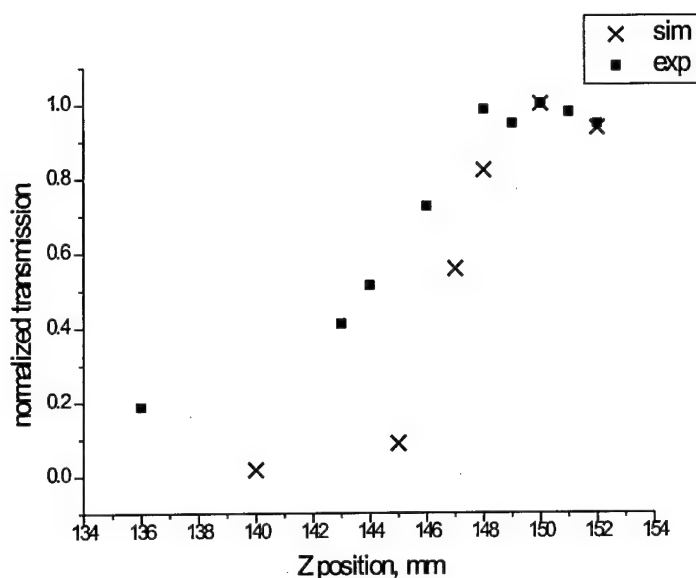


Figure 18. Variation in measured (box) and simulated (x) 20 keV transmission as the source is moved towards the lens along the fiber axis.

section, a lens actually designed for 20 keV would have a higher transmission at that energy. The primary purpose of studying this lens is to develop experience with large scale polycapillary optics and refine the modeling to increase the confidence in the simulations. The simulated and measured transmission of the lens as a function of source to lens distance is shown in Figure 18. The simulation, which models the complex geometries of complete lenses, was developed by X-ray Optical Systems, Inc. Some delay in the commencement of the simulation task was created by the necessity of assuring the confidentiality of the proprietary code while providing access to student researchers. Access has been provided, and comparisons of measurements and simulations of a collimating lens have given good results. The measured and simulated

transmission as a function of photon energy for the lens (with the central part blocked, as shown in Figure 21), is shown in Figure 22.

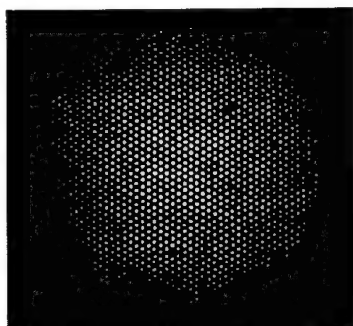


Figure 19. X-ray photograph of output of collimating optic.

More serious for imaging experiments than the low transmission of a lens designed for lower energies, is the non-uniformity of the field. The outer fibers are bent too much to permit good transmission at these energies. The fall off in transmission can be seen in the photograph shown in Figure 19, and in the simulation of Figure 20. Contrast enhancement measurements, which are ongoing, must take these nonuniformities into account. Figure 21 shows the output of the lens after a center section was blocked. This section contains fibers which were removed

diameter have been obtained. The collimating lens has an output diameter of 3 cm, a focal distance of 150 mm, and collects from an angle of 8°. It was designed for 8 keV, where the transmission is 30%, but has a transmission of 14% at 20 keV. The drop off is due to the reduction in critical angle for reflection with x-ray energy, as stated in equation (1). Because this optic would be used prepatient, low transmission would not increase dose, only increase tube loading. More importantly, as will be demonstrated in the next

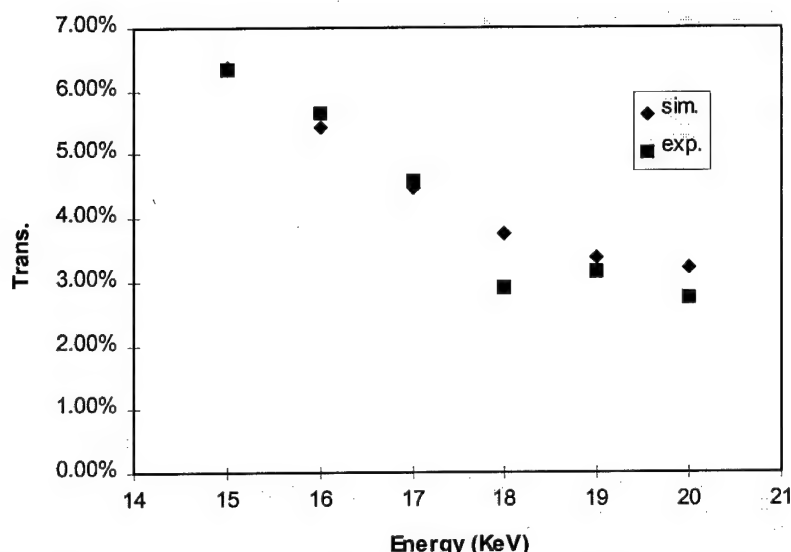


Figure 22. Transmission of 8 keV collimator as a function of photon energy. The simulation assumes a fiber open area of 65%, the fibers packed to fill 50% of the lens input area, and $\frac{1}{4}$ of the lens blocked by the lead shield..

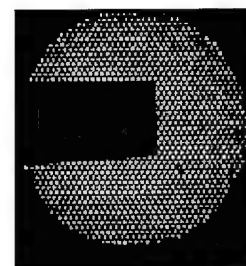


Figure 21. X-ray photograph of output of 8 keV collimator. A rectangular lead sheet blocks part of the output.

for study of radiation exposure effects after extensive exposure to intense synchrotron radiation.^{14,15} The

radiation effects were found to be manageable and are not expected to be significant for mammography.

The aligned transmission measurements of Figure 18 and Figure 22 are important to determine the collection efficiency of the lens. Variation in transmission as a function of entrance angle is important for estimating the scatter rejection properties of other optics which might be used post patient. This variation was measured by first aligning the source with the lens and then moving the source in the plane transverse to the capillary axis. The transmission efficiency decreases when the x-ray source is moved off-axis because the angle between the x ray and the reflection surface of the capillary increases. Because the reflectivity decreases sharply with angle this produces greater loss at each reflection. In addition, x rays traveling through the capillary at a larger angles undergo more reflections. A comparison of measured and simulated data, with good agreement, is shown in Figure 23. Variation in the width of the scan as a function of the lens to source distance is a method of determining both the focal distance of the lens, and the depth of field. The measured variation is plotted in Figure 24. The depth of field can also be seen in Figure 18, which shows the measured and simulated

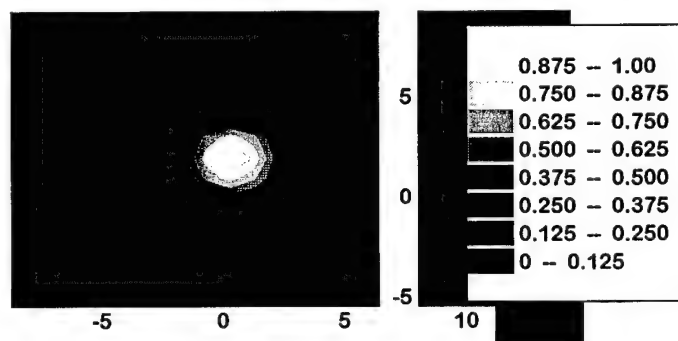


Figure 20. Simulated output, at 20 keV, of collimator designed for 8 keV.

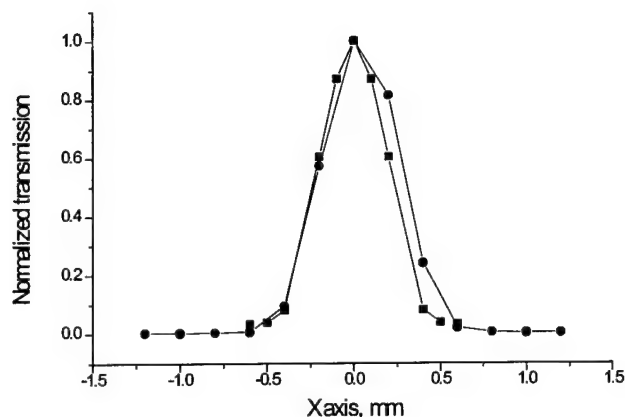


Figure 23. Transmission of a multifiber collimating lens as the source is moved transverse to the lens axis. Circles are measured data, and boxes simulation results.

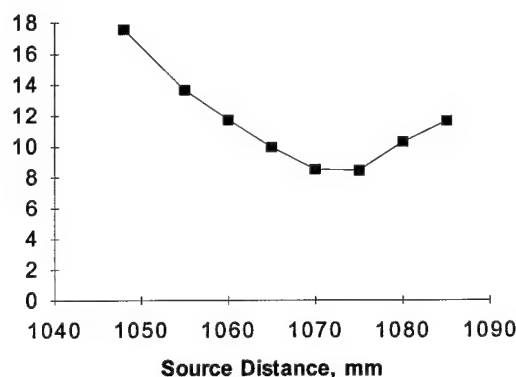


Figure 24. Width of scan of transverse source scan, as a function of source motion along the lens axis, for collimating lens, measured at 20 keV.

transmission as a function of source to lens distance. The depth of field is about 11 mm.

Measurements of the exit divergence of the collimating optic have been performed at 8 keV and at 20 keV. Exit divergence is important if a capillary optic is to be used as a collector fore slit before the patient. In this case, the spatial resolution will depend on the angular spread of x-rays at the exit end of the polycapillary fibers. Large angular divergence is equivalent to a large focal spot size in a conventional system. The full width of the divergence measured at 20 keV is 2.56 mrad, slightly greater than the critical angle for total external reflection.

The ability of the optic to redirect the collected x rays into a beam of relatively low divergence means that the reflection efficiency off a monochromatic crystal would be greatly enhanced. While the low power test source was not intense enough to permit imaging after monochromatizing, measurements were made of crystal

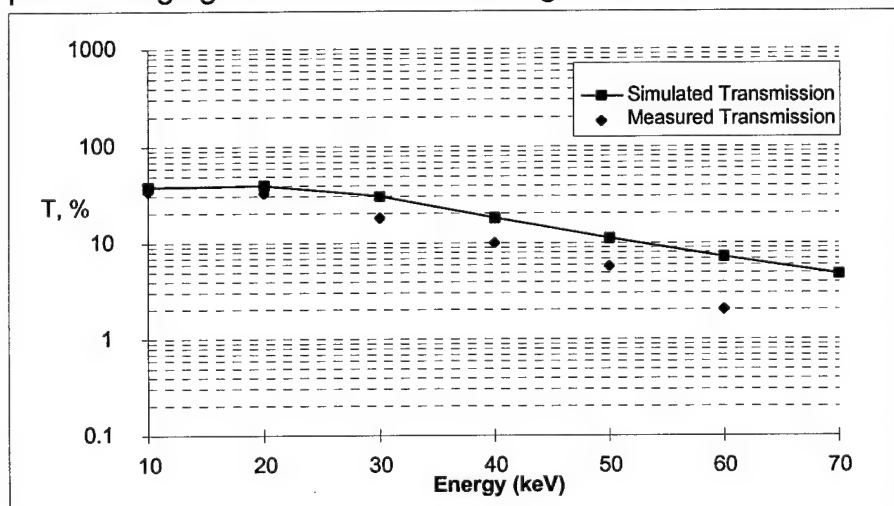


Figure 25. Simulated and measured transmission of the 20 keV prototype.

reflectivity. A silicon (100) crystal was found to reflect approximately .0047% of the beam from the molybdenum source after collimation. This is in reasonable agreement with a calculation¹⁶ of expected reflectivity for a crystal with 0.14 mrad mosaicity, which is reasonable

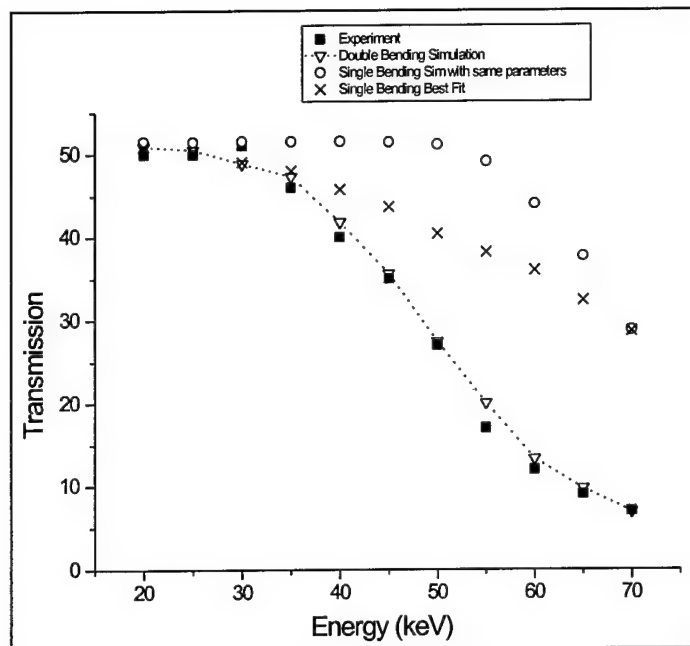


Figure 26. Transmission efficiency of a central (nominally straight) polycapillary fiber in the 20 keV prototype collimator. The fiber OD is 350 μm and the channel diameters are 10 μm . The fiber length is 14 cm. Simulated values are shown for a single bend and for a compound (double) bend. All of the simulation results assume a roughness $z = 0.3 \text{ nm}$ and waviness, $w = 0.2 \text{ mrad}$.

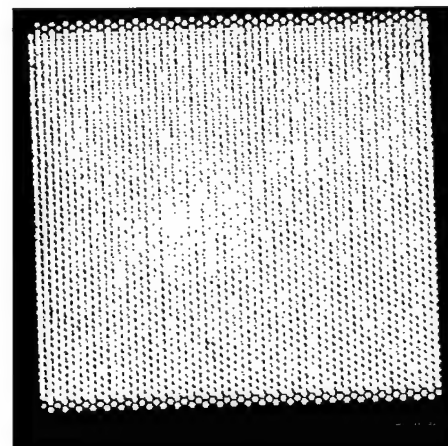


Figure 27. X-ray micrograph of 20 keV collimator, exposed 5 min at 60 keV and 0.4 mA with a W source and Polaroid film.

for the crystal used. The gain, relative to no collimation, is on the order of 1000x.

20 KEV PROTOTYPE

A second collimating lens designed for higher energies was also tested. This lens has a focal

length, 1m, which was longer than ideal for mammography, but a much larger transmission, in excess of 30% at 20 keV, as shown in Figure 25. The drop-off at higher photon energies is due to some curvature of even the central fibers, as explored in the simulation of Figure 26. The output field was also much more uniform than for the previous collimator, as shown by the picture in Figure 27 and the measurement of Figure 28. At lower exposure, in Figure 29, it can be seen that there were some defects

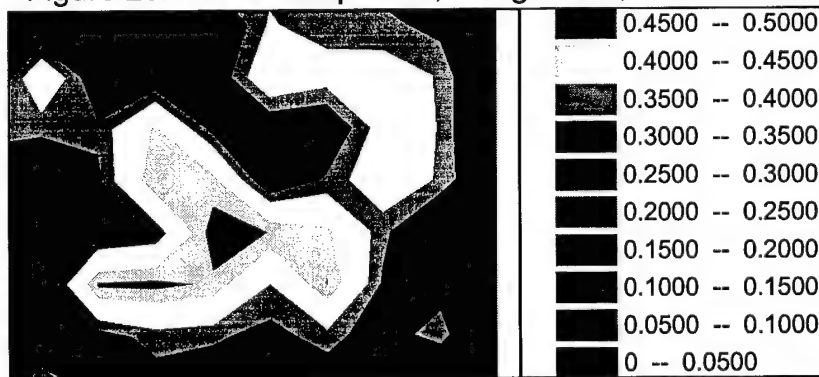


Figure 28. Output intensity distributions for the prototype TYPE I collector for different energies.

in the right half of the lens. This was due to some fiber misalignment, which was reflected in the divergence measurements. This lens was a first test of a new screen technology, which has since been improved.

Preliminary imaging measurements have been performed with the optic. Figure 31 and Figure 30 are radiographs of a 5 cm thick Lucite phantom.

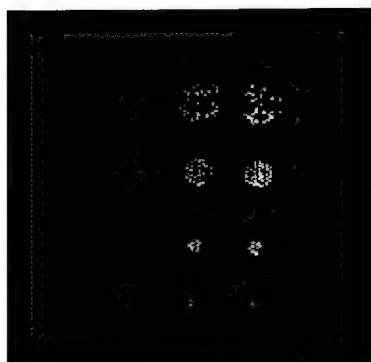


Figure 31. Polaroid film radiograph of Lucite phantom placed 5 cm from the phantom. Upper holes are 6 mm in diameter, second row is 4 mm, third, 2 mm, and fourth, 1 mm. Holes on the right are 3.5 cm deep, middle holes are 3 cm deep and holes on left are 2 cm deep.

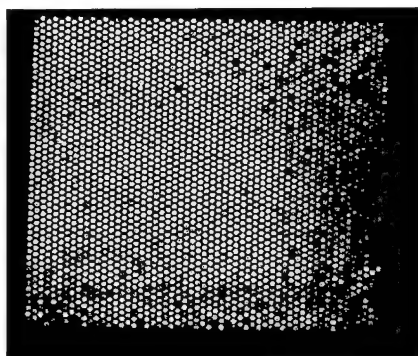


Figure 29. X-ray photograph of 20 keV collimator, exposed 5 min at 35 keV and 0.25 mA.

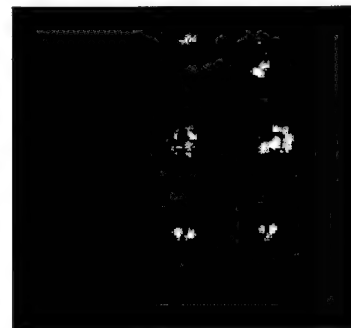


Figure 30. Polaroid film radiograph 95 cm from the phantom.

Figure 31 was taken with the film 5 cm from the phantom. Figure 30 was taken with the film 95 cm from the phantom. There is no magnification for this parallel beam geometry. However, some blurring due to fiber misalignment is observable. Given the long distance, known fiber misalignment and very low exposure the image is reasonably clear. The images were taken with normal,

x-ray insensitive Polaroid film and a very low power, 0.20 mA test source. In both cases the phantom was placed close to the output of the lens.

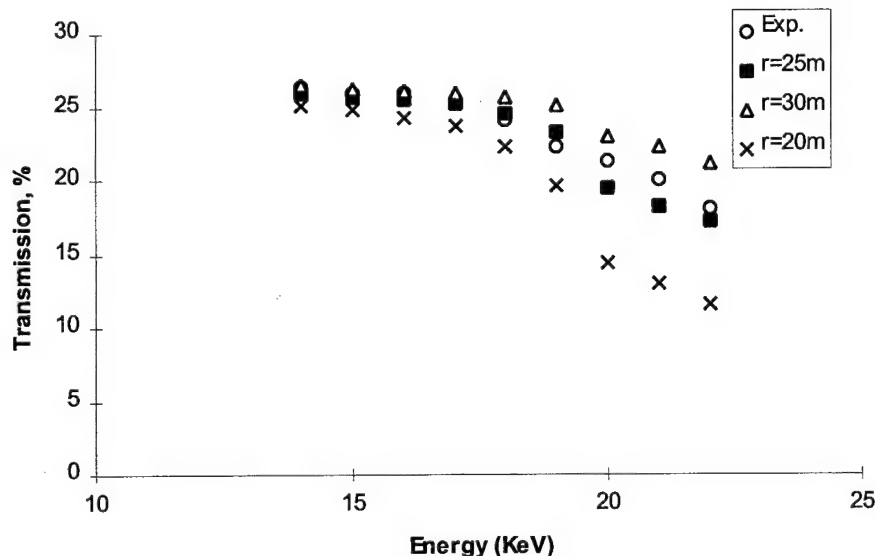


Figure 32. Simulation of straight antiscatter lens, compared to measured data. Simulation uses 1 nm roughness, 0.45 mrad waviness, and 26% overall open area.

Anti-Scatter Optics

STRAIGHT MULTIFIBER OPTIC

Rather than simply using long air gaps to eliminate scatter, as in Figure 30, a straight polycapillary antiscatter optic could be employed, as shown in Figure 17. Such an anti-scatter optic, which was essentially a 3 cm diameter bundle of straight polycapillary fibers, was aligned to the output of the 8 keV collimating lens. The anti-scatter optic was 150 mm in length with 55 μ m channels. The transmission spectrum of this optic is shown in

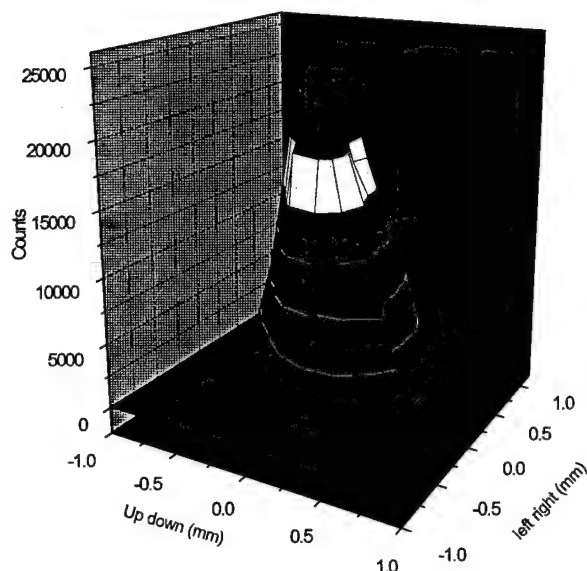


Figure 33. 2-D source scan of early prototype optic (input diameter = 2 mm, output diameter = 3 mm, transmission = 5 % at 20 keV, focal distance 22 cm) This lens transmits poorly because only the central capillary channels transmit while the outer capillaries do not transmit at all. Only about 33 % of the optic cross section transmits at 5 % or greater.

a single glass unit from input to output as shown in Figure 2 and Figure 35. These optics are relatively difficult to manufacture. Many early prototypes have poor transmission, as shown in Figure 33. To help understand the defect problem an extensive simulation and measurement study was performed on one of the better prototypes.

The focal distance of a polycapillary optic can be determined by finding the

Scanning Geometry

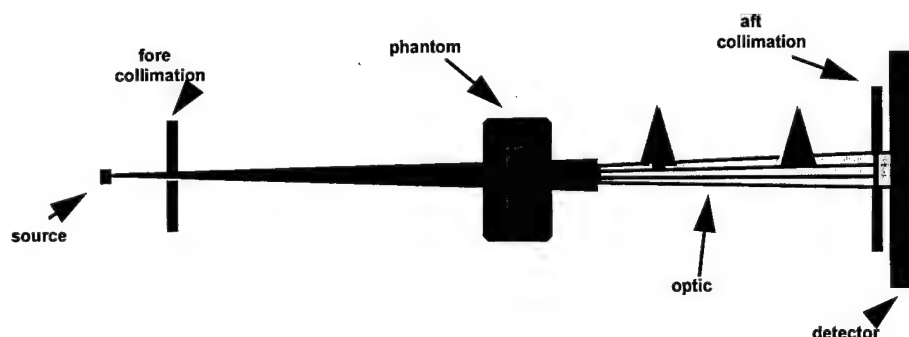


Figure 35. Small optic scanning geometry for contrast and imaging measurements.

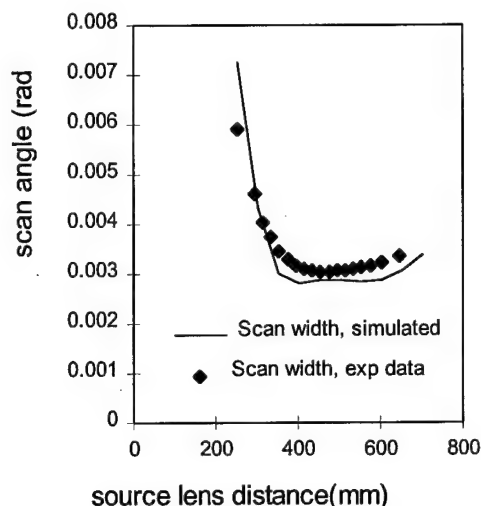


Figure 34. Source scan of tapered lens.

Figure 32. Simulations show that the apparently straight fibers have significant curvature, with radius of curvature of about 25 m.

MAGNIFYING LINEAR MONOLITHIC OPTICS

Linear monolithic optics taper as

the smallest scan angle or the maximum transmission. Source scan curves in both x (horizontal) and y (vertical) directions were recorded after the source and the lens were in alignment. FWHM of the scan curves in

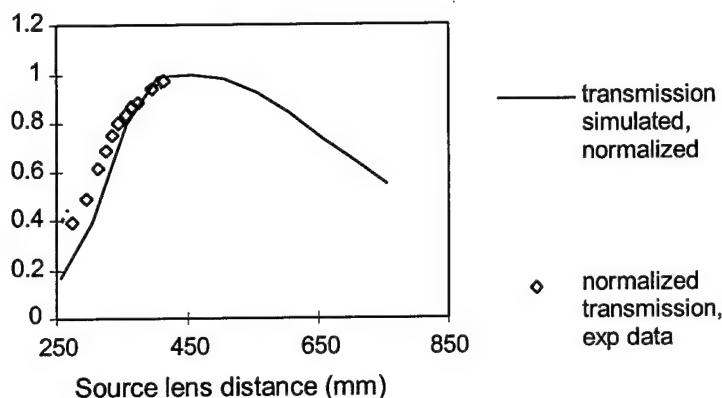


Figure 36. Transmission of tapered lens.

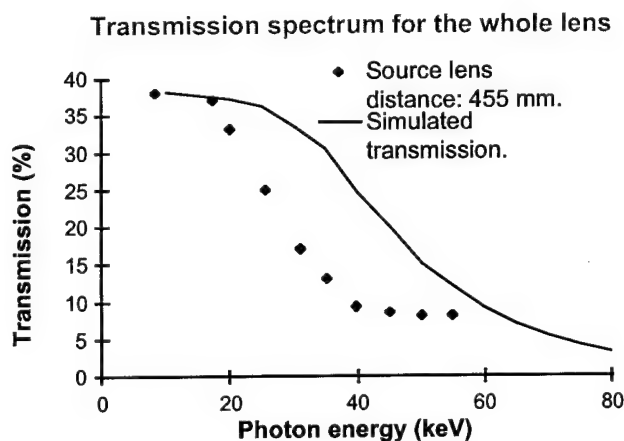


Figure 37. Transmission of whole tapered lens.

simulation values. The maximum point for transmission is around 450 mm. The second method can be affected by the source instability.

Transmission was measured in a wide energy range for the whole lens as well as the central part of the lens. The transmission spectrum for the whole lens is plotted in Figure 37. The figure shows that the transmission drops quickly for photons with energy higher than 20 keV, but the transmission under 20 keV is almost flat. The low transmission in the high energy range can be explained by the non-linearity of the lens. The outermost channels are more bent than the central channels, so they have low or zero transmission at the

both directions are calculated with Gaussian fitting, and the average FWHM is taken as the scan width at that position. Scan angle is defined as the result of the average scan width divided by the source-lens distance. In Figure 34, scan angle is plotted as a function of source lens distance. Since the theoretical curve does not have as many data points as the experimental curve, it is not as smooth as the

experimental curve. This method is not effected by the source instability, and hence is very useful when the experiment needs a long time, and the source is not stable. However the curve is quite flat near the focal distance, as expected by simulation. The scan widths have to be measured very carefully to determine the focal distance. The focal distance determined by minimizing the scan angle is 455 mm for this lens. Transmission and photon counts are also plotted versus source lens distance in Figure 36 along with the

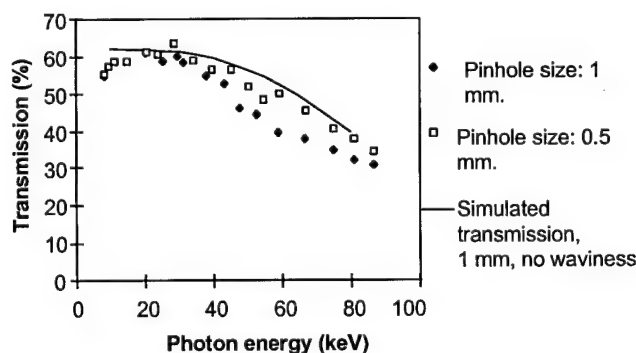


Figure 38. Transmission of the central part of the tapered optic.

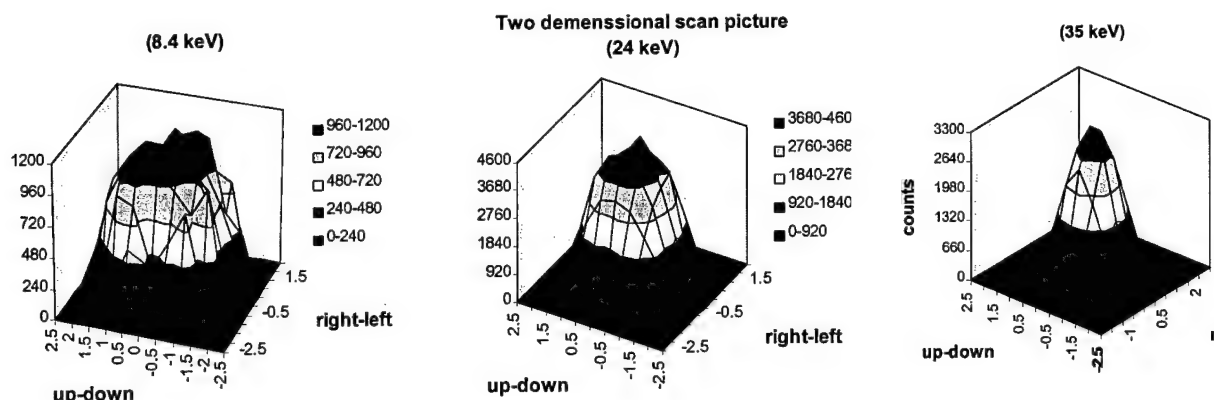


Figure 39. Two dimensional scans of the output of the tapered optic.

higher photon energies. This is confirmed by the higher transmission measurement at the central part of the lens, shown in Figure 38 and the transmission uniformity measurement at different energies, shown in Figure 39. Transmission uniformity of the lens was measured by putting a 200 μm pinhole in front of the lens and performing a two dimensional scan. At 8 keV, the whole lens transmits, although we can see the transmission is not completely flat due to the non-linearity and the defects of the lens, such as blocked channels. At 25 keV, transmission of the whole lens drops to 25%. Most of the lens is still transmitting at 25 keV, but the outer channels have lower transmission than the central part. At 35 keV, the lens has a narrower transmitting region. The measurements show that the lens has undesirable nonlinearity.

Simulations plotted in Figure 36 and Figure 37 as the solid lines assume when the lens is uniformly bent. The simulations used the same roughness and waviness correction as that used for fiber D in Figure 5. A linear tapered lens is ideal for mammography, because, as shown above, any curvature can cause transmission reductions. However, the lens currently available has a nonlinear profile. The profile is not circular, but to simplify the simulation, we assume that the profile is circular. A uniform bending will provide the best transmission performance for a given bending angle, so the simulation will overestimate the lens performance. A further simplification assumes the lens has a fixed channel size, although the channels actually taper with the lens. A more sophisticated lens simulation program is under development.

The geometry for uniformly bent nonlinear lenses is shown in Figure 40. The

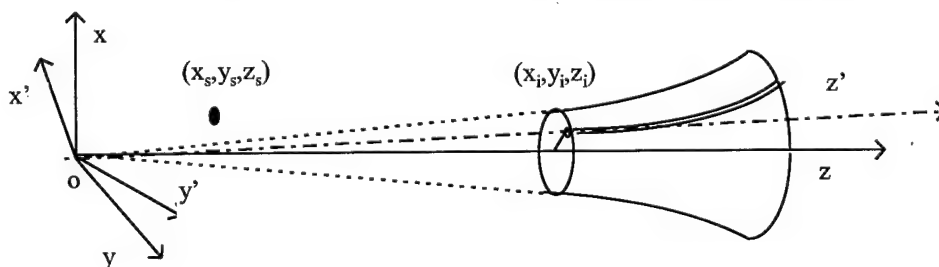


Figure 40. Geometry for Lens simulation.

simulation method for a uniformly bent lens is an extension of the simulation for uniformly bent polycapillary fibers. The simulation is

done by sampling channels in the input cross section of the lens with an even step size. In the simulation for a bent fiber it is assumed that the capillary bends in -y direction, and z direction are along the input axis of the fiber. In order to reuse the old simulation code, the coordinate of the simulation x-y-z is rotated to x'-y'-z', where z' is the direction of channel axis at the input end and -y' is the channel bending direction. Assume the source position and the capillary position at input end is (x_s', y_s', z_s') and $(0, 0, z_i')$ respectively, then the source capillary distance is $z_i' - z_s'$. The origin of the coordinate is selected to be the focus point of the lens.

Another parameter needed by the simulation is the bending curvature of the selected channel. This value varies with the position of the channel. The calculation of the bending curvature is demonstrated in Figure 41.

First it is assumed that the channels are evenly distributed on both input and output cross section. Let input and output diameter of the lens be r_i and r_o , and focal distance \overline{OA} be f , and the lens length \overline{AC} be L , then

$$\overline{AB} = \sqrt{x_i^2 + y_i^2}, \quad \overline{CE} = \overline{AB} * r_o / r_i$$

$$f / (f + L) = \overline{AB} / \overline{CD}, \quad d = \overline{CE} - \overline{CD}$$

For a small bending angle,

$$\alpha \approx L / R = d / (L / 2)$$

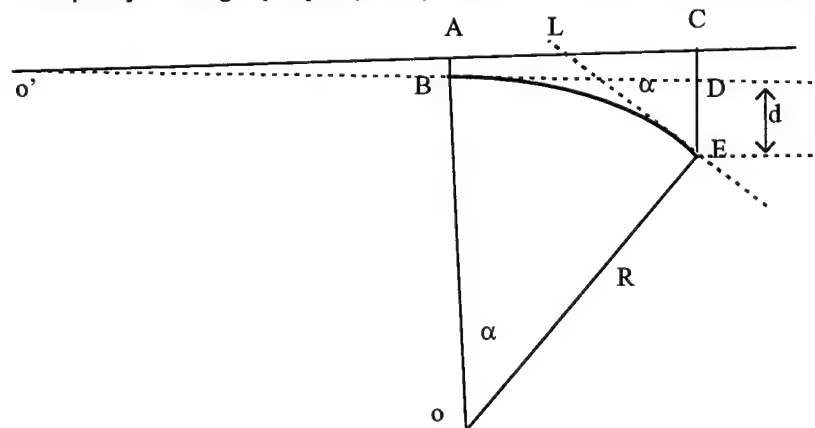
where R is the bending radius, d is the distance between point D and E as shown in Figure 41, and α is the bending angle. Thus

$$R = L^2 / 2d \quad (1)$$

The simulated results in both cases show higher transmission than the experimental results. This indicates that the lens has more reduction in transmission due to the bending. This is expected, because the lens does not have a uniform bending.

Manufacturing Issues

The only practical method to produce larger optics is to couple several smaller optics together to form one large optical component. The method we propose to attach the individual optical elements together is quite similar to the method that is used by the company to align polycapillary fibers. These polycapillary devices consist of thousands



of individual polycapillary fibers that are strung through rigid grids to produce a single large optic. The individual fibers must be aligned to within a few microns in position and to less than a milliradian in angular orientation. These requirements are more stringent than those required in this project. The alignment technology is not

Figure 41. Curvature estimation for lens simulation.

likely to be a problem. However, first high quality monolithic tapers must be reproducibly manufactured.

XOS has developed the capability to make long tapers with diameters up to 5 mm with transmission which indicate the future potential, but which is currently less than half the expected value. Work is necessary to improve profile control (linearity), increase transmission efficiency, and increase achievable optic diameter. Single examples have been manufactured which demonstrates sufficiently good performance to support the medical imaging research and demonstrate the feasibility of the approach. However, considerable work is necessary to achieve optics suitable for clinical use.

There has been substantial progress in achieving the necessary manufacturing control to repeatable produce high quality optics. In recent, the current manufacturing technique was carefully studied, the critical problems were identified, and a plan was

Table 3

PROBLEMS	ACTION NECESSARY
<ul style="list-style-type: none"> decrease in open area 	<ul style="list-style-type: none"> better temperature profile control better tension control evaluate tension - temperature trade off
<ul style="list-style-type: none"> inclusions, primarily glass particles 	<ul style="list-style-type: none"> improved handling and bundle assembly procedures static electricity abatement including controlling for humidity laminar flow hoods
<ul style="list-style-type: none"> cast (curvature) 	<ul style="list-style-type: none"> improved alignment of feed mechanism, furnace, and puller radially symmetric uniformity of heat zone longer cooling zone better control of air flow
<ul style="list-style-type: none"> OD control 	<ul style="list-style-type: none"> improved temperature and tension control real time monitoring of OD with closed loop feedback
<ul style="list-style-type: none"> waviness in glass surface 	<ul style="list-style-type: none"> elimination of internal vibration sources, e.g., friction, motors being operated slower than designed, turbulent forced air cooling isolate from external vibration sources change to cutter approach which doesn't cause large periodic shocks more homogenous glass (optical quality)

prepared to modify the manufacturing process. The first step was to increase the controllability and reproducibility of the manufacturing process. The development of monitoring automation and feedback systems was achieved. As a result of the improvement in process control, systematic and rapid improvement has been made in the development and manufacturing of new optics.

Initially, glass preforms and prototype optics were produced in Russia. They were of relatively poor quality, and no two optics were equivalent in performance, but they served as proof-of-principle devices. Because of the technical and political difficulties, Russian optics and preforms are no longer available. When it became apparent that having the optics manufactured in Russia was not viable long term, X-Ray Optical Systems, Inc. (XOS) commenced developing a U.S. manufacturing capability.

XOS chose to work with the polycapillary subcontractor that has the best controlled process for making polycapillaries which work well at 8 keV. The glass is formed by a continuous, steady state, vertical pulling process, with as much as 1,000 meters in a single production run. Several manufacturing runs were conducted with evaluations of the polycapillaries done between each run. Adjustments to the process were made for each new run. XOS personnel participated in some of the runs. The polycapillary performance and the manufacturing process were carefully analyzed to determine what changes were needed in manufacturing to obtain the desired polycapillary capabilities. This manufacturer does not use computer control. There was no automatic feedback in the manufacturing system. The system was controlled by having an operator observe that a condition such as the outer diameter of the polycapillary or the furnace temperature had drifted from the desired point and then manually adjusting one of the control variables. The polycapillary performance at high energies was not acceptable. Problems which were identified, and the actions determined to be necessary are identified in the Table 3. XOS determined that this supplier was not able and/or willing to make the necessary equipment, personnel, and operational changes. With this information, XOS modified an in-house glass pulling system to investigate the effect of making some of the changes which were determined to be necessary.

A systematic evaluation the major manufacturing parameters was not possible initially as the first prototypes made were pulled on a setup where there was little control over the manufacturing parameters, and little ability to record the parameters during the forming process. The initial setup was put together inexpensively to provide some indication of the direction to proceed. It enabled a definition of a general range for some of the manufacturing parameters, such as pulling speed, so that acquired information could be used to design a more sophisticated pulling setup. One source of variation in the prototype monolithic optics came from the uncontrolled air flow through the furnace.

Modeling of the optic shaping process was conducted. Modeling provides some understanding of the underlying relationships between the manufacturing parameters and the resulting optic. Constant feedback of the experimental results to increase the accuracy of the model is an important input to the scientific, quality, and production methods. The modeling is based on a one-dimensional finite-differences algorithm.

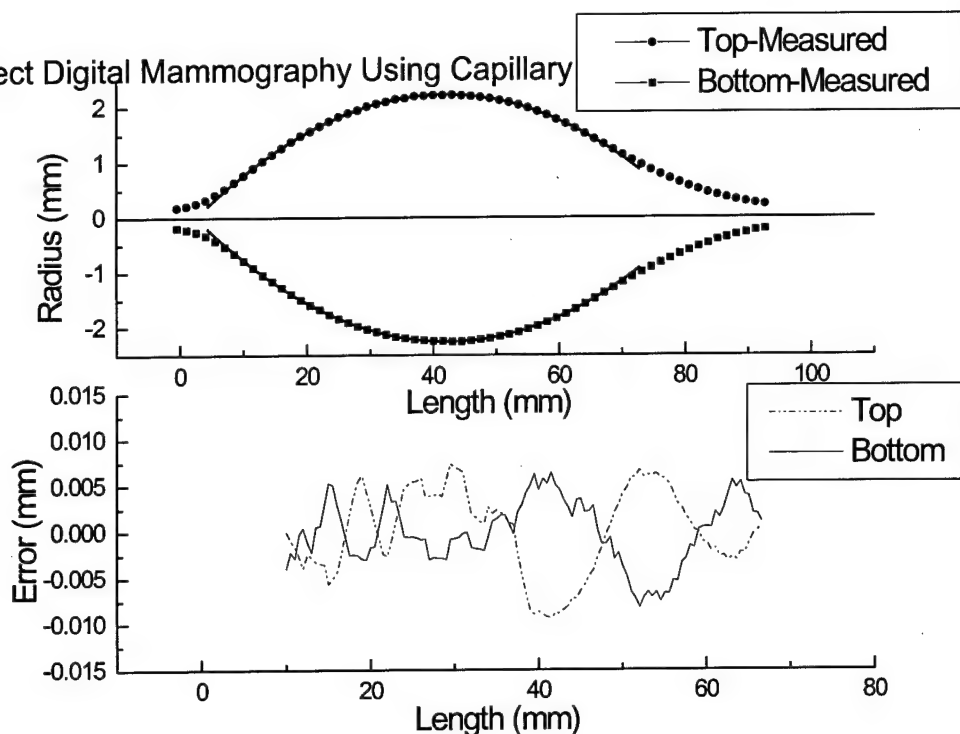


Figure 42. Variation in optic profile, compared to design.

The preform (large outside diameter polycapillary bundle) is split into finite elements. This approach allows the thermal and mechanical properties of each segment to be calculated. At each time step, the ends of the preform are moved according to a predetermined, but likely variable, speed. The formation of the lens occurs in the heated area and the glass will flow according to viscosities. Since the total volume of each element is kept the same, the elements that are stretched the most end up with the smallest diameter. The radiative heating by the furnace as well as radiative cooling from the preform must be considered. The thermal profile for the preform can be calculated for points along the center axis of the furnace.

A second generation pulling tower was constructed and instrumented to allow flexibility in controlling different parameters and to record the actual status of parameters during the pulling. The tower uses servo motors with encoders to displace the preform and furnace; multiple thermocouples to monitor the temperatures; and load cells to monitor the pulling forces. So far a few long tapered monolithic optics have been formed using this system. There are numerous independent and dependent variables that effect the quality and reproducibility of a lens design. In addition to the parameters already known to effect the reproducibility and quality of the lens, it is expected that others will be revealed. An important part of the project will be to establish the relative importance of each parameter through a systematic, multivariable experimental approach. The goal being to seek a rapid high-quality path to large tapered monolithic polycapillary lens production. Several of the development steps will proceed concurrently. An example of this is the storage, treatment, and holding methods of the preforms can be investigated while the lens formation process is proceeding through its initial data collection and analysis steps. Although the ultimate quality of the lens is dependent on each of these paths, the synergism is likely not realized until the relative significance of the basics is established. The preform material

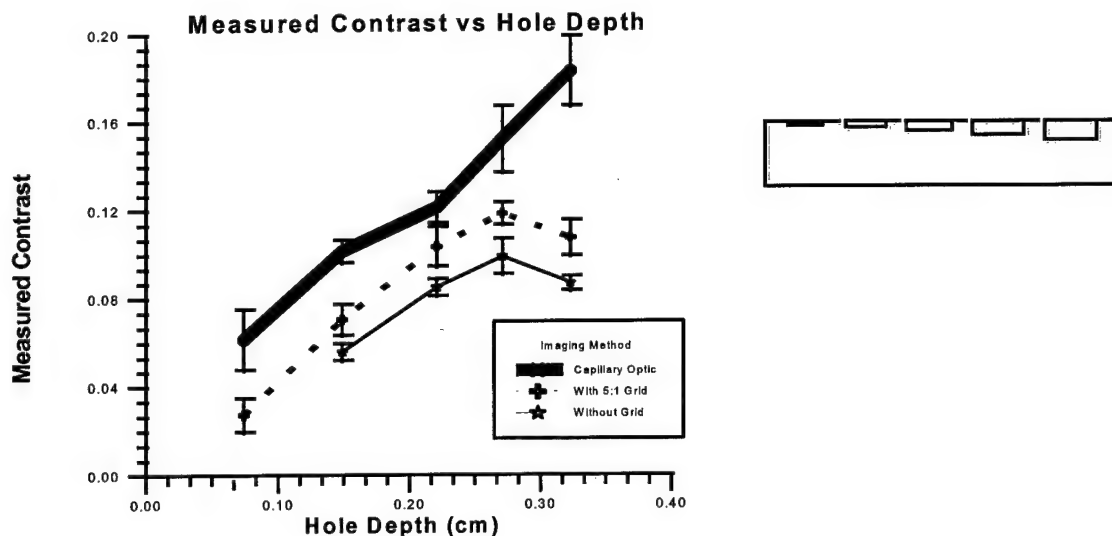


Figure 43. Contrast enhancement measured for a small scanned capillary optics using a phantom consisting of a Lucite block with drilled holes.

will be characterized for open area, x-ray transmission, uniformity of outside diameter. General observations of the presence of inclusions, cleanliness, and uniformity of color will be noted. Then the appropriate method of storage prior to use needs to be investigated. Precautions to protect the material from dust and moisture will be taken.

There is a strong interdependence of tension on the preform, temperature in the various heating zones, speed of the pull, and mechanical feedback. Extensive correlation of the data from the forming process with the lens performance will be needed to optimize the system. Additional considerations include the heat capacity of the glass and time-temperature response of the furnace. Uniformity of gas flow through and around the glass during the pulling step is important to monitor. To assure

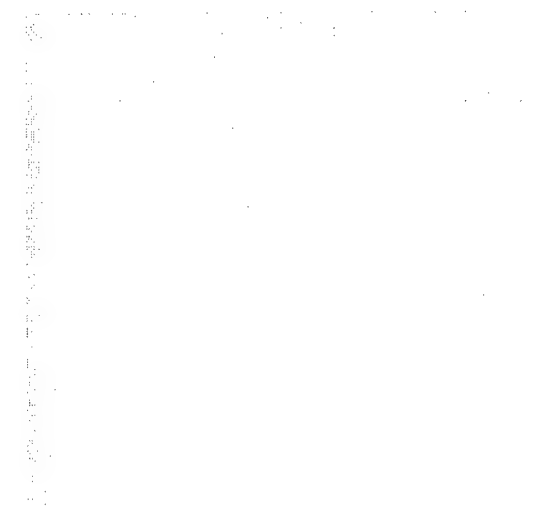


Figure 44. Image of contrast phantom produced with conventional grid.

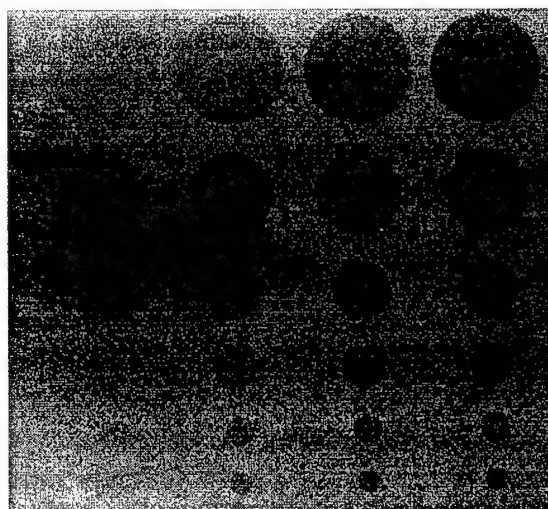


Figure 45. Image of contrast phantom produced with capillary optic.

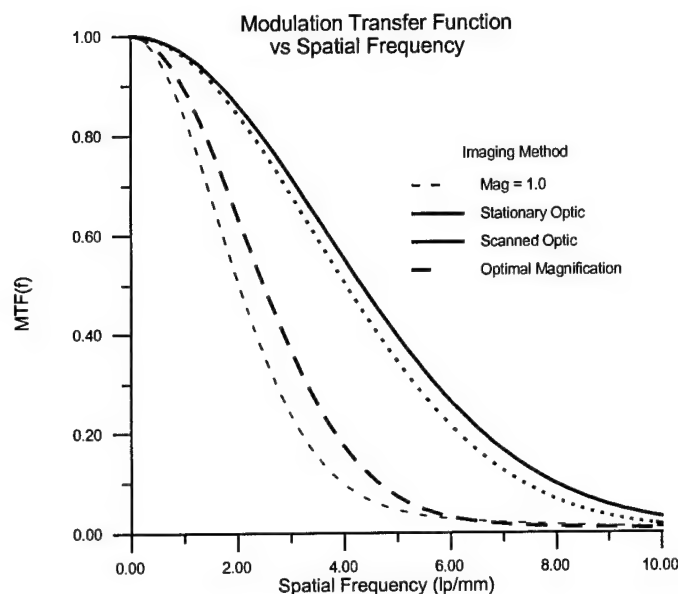


Figure 46. Modulation Transfer Frequency measurement with and without the optic.

In fact, most will not become an issue of concern until the grosser variable are better controlled. Already, by experience and through our interaction with consultants, XOS has made significant progress in the design and construction of monolithic polycapillary optics.

One example is a set of 17 keV focusing optics designed for microfluorescence analysis. The profile of the optic was measured with a microscope-based MicroVu video coordinate measuring system at XOS. The precision of the system is about 5 μm . Figure 42 shows the measured profile compared with the design profile. Deviations along the optic axis between the two profiles are also shown in Figure 42. Less than $\pm 10 \mu\text{m}$ deviation represents the current manufacturing precision.

Imaging Measurements

To overcome the manufacturing difficulty inherent in producing large diameter monolithic optics, the design decision has been made to concentrate on small scale prototypes which might be assembled into a large optic using a technique similar to that used to produce multifiber lenses.

Contrast enhancement measurements have been performed with a small scale (2 mm diameter) optic as part of an on-going collaboration with the Univ. of Wisconsin.¹⁷ The geometry for the scan is shown in Figure 35, and the resulting contrast enhancement compared to the no optic and conventional grid cases are shown in Figure 43. An image made with a conventional grid and with a scanned optic are shown in Figure 44 and Figure 45. Improvements have been made in the scanning system to reduce image artifacts. Scan lines which were visible in previous images are not apparent in Figure 45.

uniformity and appropriate use of heat zones, other parameters to consider include: baffling, furnace diameter, and correlation of furnace motion with the movement (i.e. flow) of the preform. In a motor driven system, there are vibrations, motor inertia, slew rates, as well as bearing, slide, and belt qualities that must be evaluated. Other mechanical conditions to evaluate include how the preforms are held and supported to maintain uniform alignment and minimize random and systematic perturbations. Despite the number of parameters to be considered, only a few are thought to be critical to first order, others affect the quality in diminishing amounts.

The optic was also used to measure the resolution enhancement due to magnification. A plot of the measured MTF is shown in Figure 46. At the 0.1 MTF level, the resolution improved from 4.5 lp/mm² without the optic to 8.9 lp/mm² with the optic.

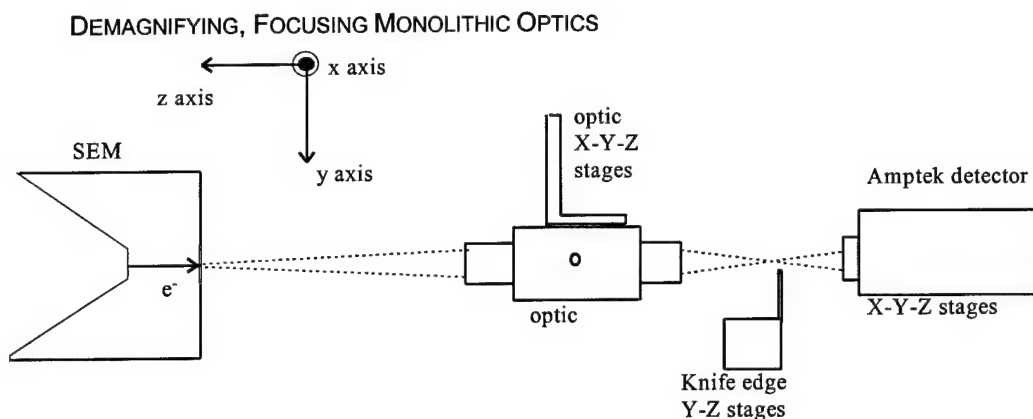


Figure 47. Schematic of the experimental setup for optic characterization.

Monolithic optics similar to the collimating optic shown in can be used to minify an x-ray beam. Some characterization of such optics has been performed. The first measurement characterized an optic using a point source, a micro-focused transmission x-ray source (spot diameter about 5 :m) modified from an old SEM. Anode materials made of Cu and Mo are coated on a thin Be vacuum window. An energy-sensitive Amptek detector with an energy resolution of 250 eV at 5.9 keV was used for x-ray detection. The crystal size of the detector is 7 mm². The detector was placed roughly at the output focal plane of the optic, 8.5 mm away from the exit of the optic, to allow the detection of the output beam from the entire optic. The polycapillary focusing optic and detector were mounted on x-y-z stages which allows precise alignments among the source, optic, and detector. Figure 47 shows the schematic of the experimental setup. The alignment of the optic input focus to the source is achieved by moving the optic in all three orthogonal directions until the transmitted flux is maximized.

The output focal spot of the prototype optic was at Cu K_α and Mo K_α. The measurement was performed by scanning a tungsten knife edge plate across the

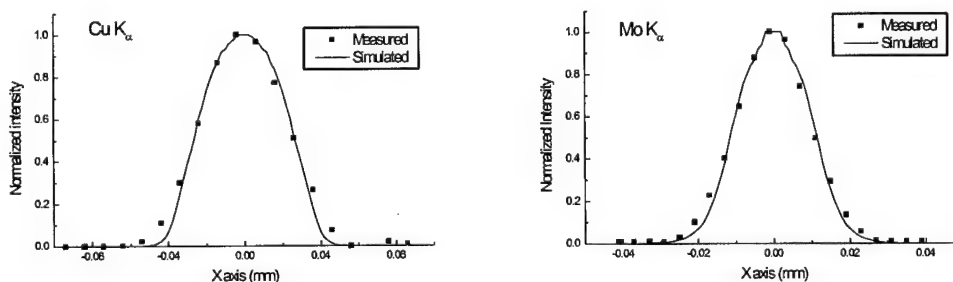


Figure 48. Focal spot scans of focusing optic.

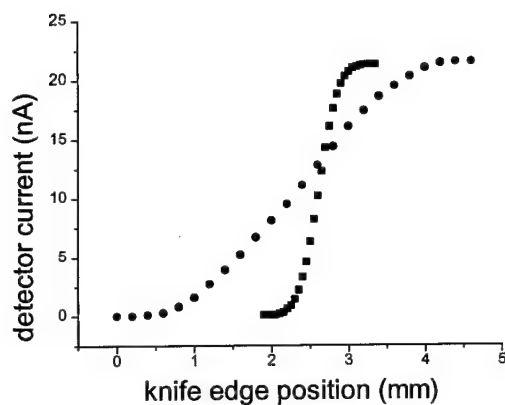


Figure 49. Knife edge scan at a knife edge to source scan distance of 103.5 (●) and 123.5 mm (■).

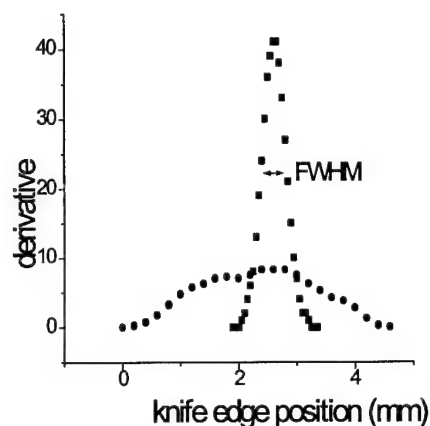


Figure 50. Derivative of knife edge scan for optic to knife edge distances of 103.5 mm (●) and 123.5 mm (■).

focused beam on the focal plane. The first derivative of the measured intensity as a function of the position of the knife edge gives the intensity distribution of the focused beam. This is shown in Figure 48, with the simulation results as comparisons. Good agreement between the measurements and the simulations indicate good alignment of the capillaries toward the output focus and that the simulation can reliably predict the divergence of the output beams from the capillaries. The measured spot sizes (FWHM) are 44 μm for Cu K_α and 21 μm for Mo K_α , respectively.

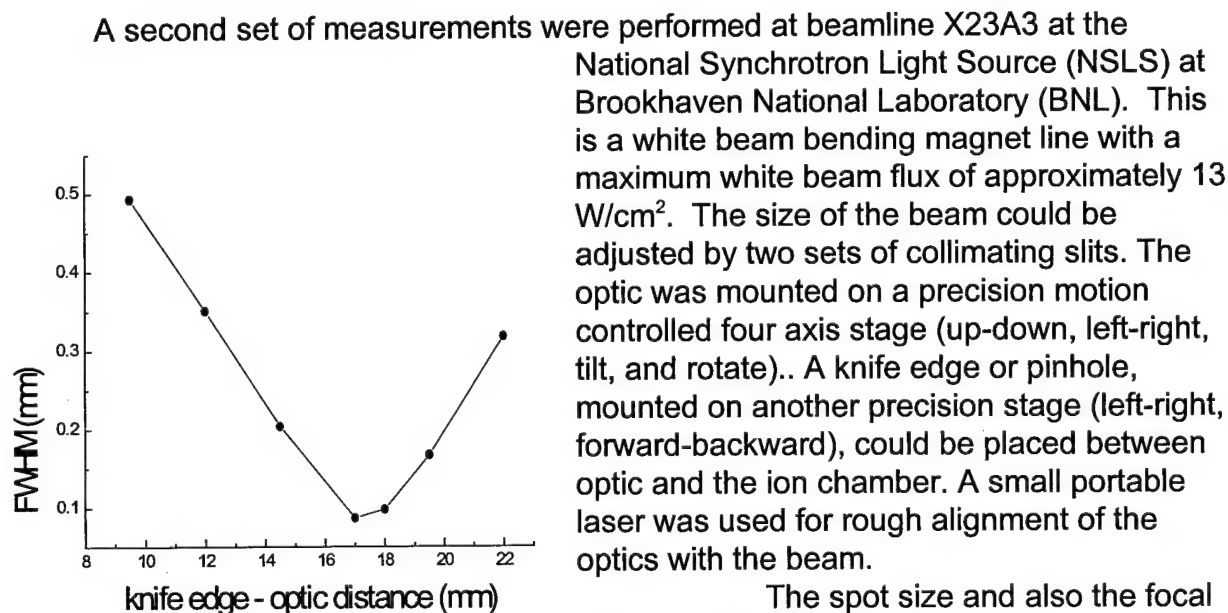


Figure 51. Width of derivative of knife-edge scan versus distance to optic for monolithic optic.

A second set of measurements were performed at beamline X23A3 at the National Synchrotron Light Source (NSLS) at Brookhaven National Laboratory (BNL). This is a white beam bending magnet line with a maximum white beam flux of approximately 13 W/cm^2 . The size of the beam could be adjusted by two sets of collimating slits. The optic was mounted on a precision motion controlled four axis stage (up-down, left-right, tilt, and rotate). A knife edge or pinhole, mounted on another precision stage (left-right, forward-backward), could be placed between optic and the ion chamber. A small portable laser was used for rough alignment of the optics with the beam.

The spot size and also the focal distance were measured using a knife edge that was scanned horizontally across the beam. Two scans, one near to the focal spot of the multifiber optic and one 20 mm closer to

Table 4. Results for monolithic focusing optic.

X-Ray Energy (keV)	Spot size (mm)	Transmission (%)	measured Gain for 350 μ m pinhole	calculated Gain 350 μ m pinhole	calculated Gain 90 μ m pinhole	calculated Gain 10 μ m pinhole
6	0.09	36	78	81	645	911
8	0.08	49	96	110	933	1359
10	0.09	39	83	87	624	842
12	0.09	39	74	87	654	903
white	0.17	42	11	89	243	266

the optic, are shown in Figure 49. The derivatives of these scans are shown in Figure 50. The scan close to the focal spot has a smaller width than the scan far away from the focal spot. A plot of the width of the scan derivative as a function of distance from the multifiber optic is given in Figure 51. Resulting calculated and measured gains are shown in table 4

Direct Digital Detectors

CZT Detector

Digirad, Inc. (formerly Aurora Technologies) was somewhat delayed by the late start date of their subcontract with the University at Albany due to contract formalities. However, a 1 cm long CZT array with 50 μ m pixels has been manufactured and tested. The interconnect options were researched and the decision was reached to employ indium bump technology to bond the detector to a sapphire or quartz interconnect board, which is then bonded to the readout chips. This approach eliminates the need to wirebond to the detector, and also reduces the pixel size and consequently the leakage current. The first prototype has demonstrated some mechanical instability. It is believed this is fixable with epoxy.

Measurements of room temperature energy bandwidth, detector quantum

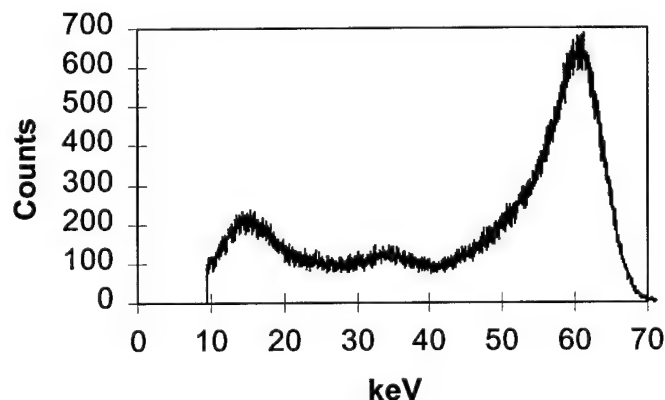


Figure 52. Spectrum from Am 241 taken with CZT single pixel detector.

efficiency, and response uniformity were performed with a single pixel bulk CZT detector. Measurements of pixel to pixel variation using a scanned slit were performed with a linear CZT array.

Single pixel CZT detector

A single pixel detector 5.0 mm x 5.0 mm in area and 1.5 mm in thickness was used for the measurements. The external aluminum window was removed for the detector quantum efficiency measurement.

The spectrum produced by

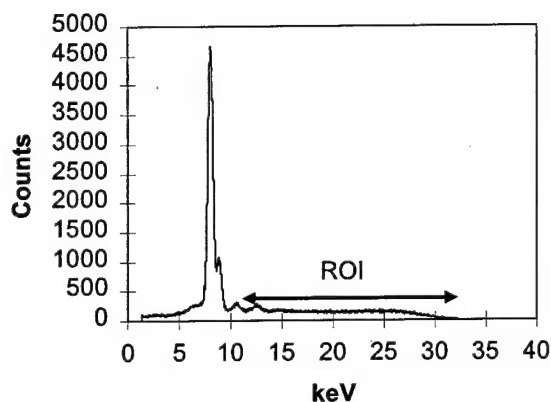


Figure 54. Spectrum of copper x-ray source, taken with HpGe detector. Lines at 10.5 and 12.6 keV are lead fluorescence from shielding. The region of interest (ROI) is marked.

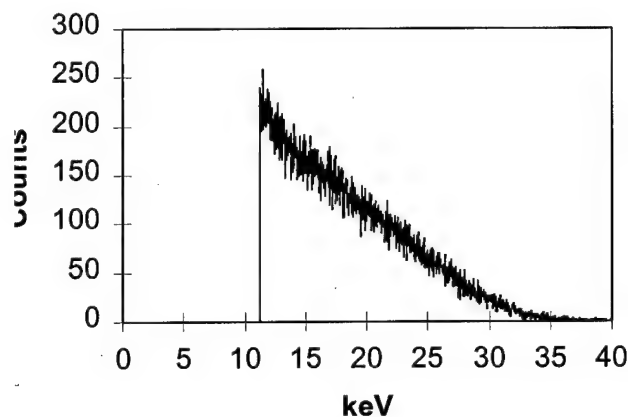


Figure 53. Spectrum of copper x-ray source, taken with single pixel CZT detector. The lower level discriminator was set at the lower end of the region of interest (ROI) marked in figure 5.

the CZT single pixel detector with a Am-241 radioactive source is shown in Figure 52. The spectrum was obtained with a Tennelec TC 241 linear preamplifier connected to a PCA-Multiport multichannel analyzer. The noise threshold at room temperature with this preamplifier is 10 keV. The FWHM of the Am 59.54 keV gamma is 9.5 keV at room temperature. The 17 and 24 keV lines of Am could not be resolved.

The detector quantum efficiency was measured in comparison to a high purity germanium (HpGe) detector with a 13 mm thick, 36 mm diameter crystal. For the HpGe detector, the efficiency was considered to be equal to unity in the energy range in which the experiment was performed. This detector was connected to the same linear amplifier and multichannel analyzer as the CZT detector. The distance between the source and the 100 μm pinhole was 50 cm. The distance was chosen to maintain dead times less than 10%. The distance between the plane of the pinhole and the detectors was kept equal to 5 mm for both

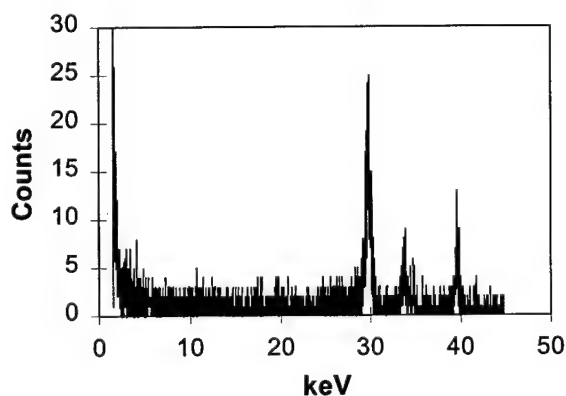


Figure 55. Spectrum from radioactive iodine taken with HpGe detector.

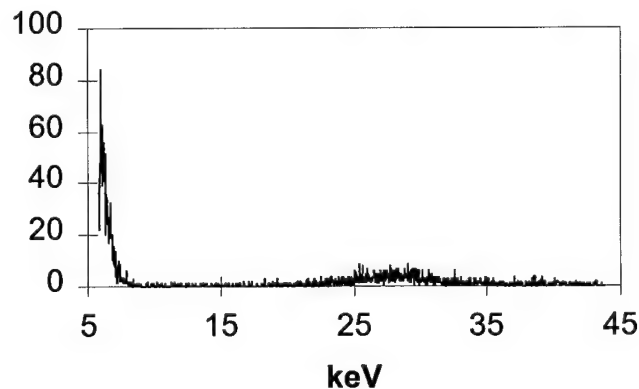


Figure 56. Spectrum from radioactive iodine taken with CZT detector

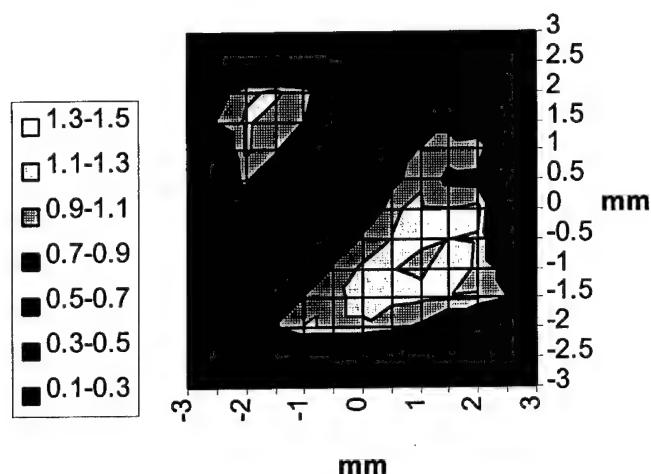


Figure 57. Pinhole scan of CZT single pixel with band of contact material.

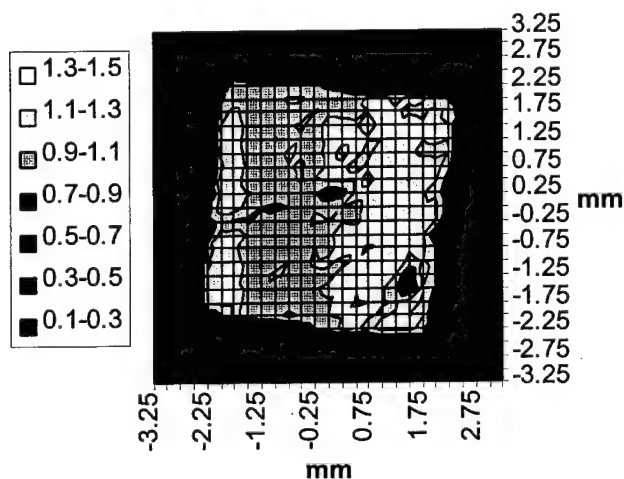


Figure 58. Pinhole scan of CZT single pixel.

detectors, which was as small as possible given the HpGe detector geometry. The small separation reduces the effects of scattered or fluorescent radiation and ensures that the entire beam exiting the pinhole is intercepted by the detector. The HpGe detector was calibrated in energy using the Am gamma and the 5.9 keV line of Fe 55. The CZT detector was calibrated using the Am 59.54 keV line and a pulser set to equal and to half-height of this line.

Two different x-ray sources were used for this measurement. First was a copper x-ray tube with tube voltage of 30 kV, with the spectrum, obtained with the HpGe detector, shown in Figure 54. The resultant CZT spectrum for the same count time is shown in Figure 53. Interpretation of the results is complicated by two factors. First, the noise threshold, and therefore the lower level discriminator, is above the peak of the spectrum, so only the higher energy bremsstrahlung is recorded. Second, monoenergetic high energy photons, due to hole tailing effects, contribute to counts in a long Laurencian tail to lower energies, as seen for the Am gamma in Figure 52. Therefore counts due to photons

with energy above the threshold are lost into lower energy channels. The detected quantum efficiency for this source, determined roughly as the ratio of integrated counts in the regions of interest shown in Figure 54 and Figure 53, was found to be 44 %. A similar measurement was performed for a radioactive iodine source, with the spectra shown in Figure 55 and Figure 56. The DQE for this source is 42%. An imaging detector, which counts events independent of energy, would be affected by the hole-tailing only to the extent that the ends of the tail are below the noise threshold.

Area uniformity measurements were performed on a bulk single pixel detector by scanning the active area of the detector with a 300 μm pinhole. The result for the first detector tested is shown in Figure 57. The diagonal band is a strip of contact material normally unimportant for the operation of this detector in the infrared. The scan of a

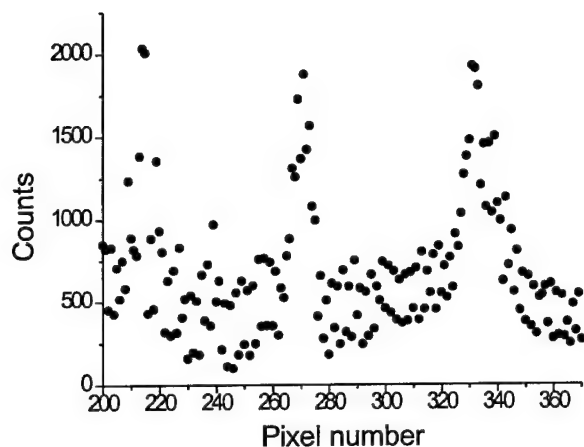


Figure 59. Image of slit taken with linear CZT array, without background subtraction.

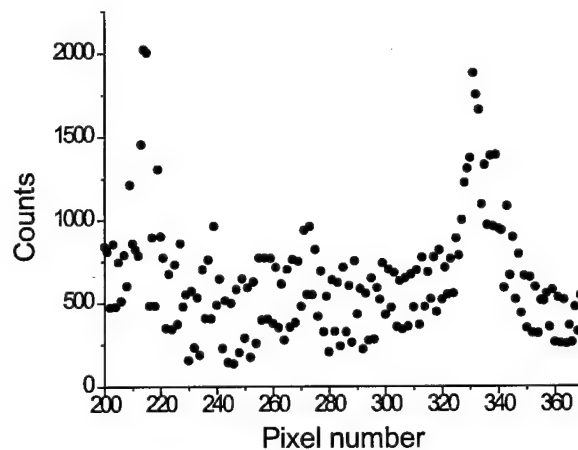


Figure 60. Background associated with image in figure 11.

second detector, produced without this contact material, is shown in Figure 58. The average count rate in the 3.5 mm central area was normalized to unity. The variance in that region is 8%, 3% of which is due to Poisson statistics. Some part of the variance (4%) is due to the external aluminum window. The semiconductor sensitivity is quite uniform over the entire pixel.

Linear array

The CZT linear array was attached to the read-out electronics by means of indium bump bonding technology. Measurements were performed only for the central pixels because mechanical stresses caused bonding failure for the end pixels. This will be corrected for future arrays with an addition of epoxy for mechanical adhesion. To check the uniformity of the response of the pixels to x-ray radiation, a 0.5 mm slit was placed between the detector and the copper x-ray source. The array was then mounted on a translation stage that allowed movement parallel to the plane of the slit. The result without background subtraction is shown in Figure 59. The background,

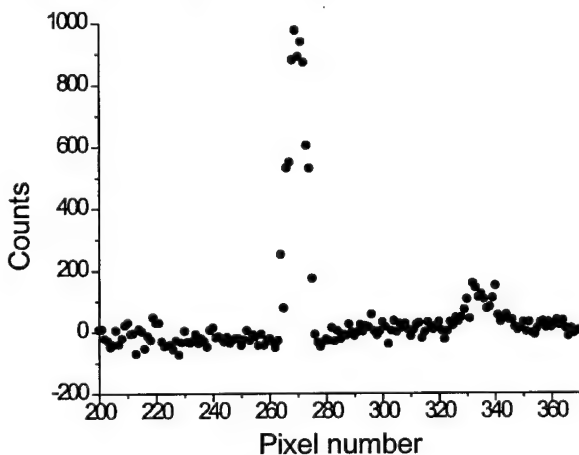


Figure 62. Slit image from Figure 64 with background from Figure 63 subtracted.

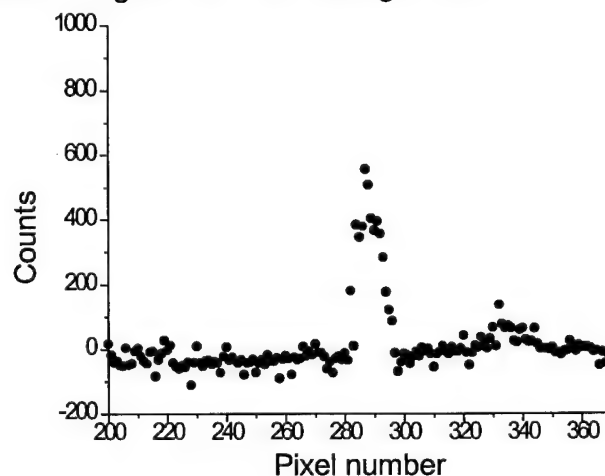


Figure 61. Background subtracted image of slit after moving detector to the left.

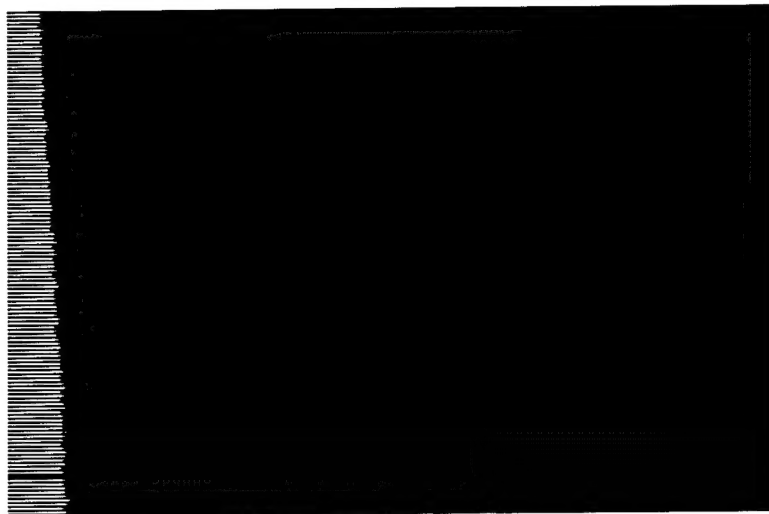


Figure 63. CID image of three grids. The largest has open spaces 560 microns wide and 300 micron wires. The smallest, unresolved at upper right, has 25 micron holes. The grid at center has 50 micron holes. The image was taken with magnification 1.02 onto the chip, which has 28 μm pixels.

counted for the same period without the source on, is shown in Figure 60. The background subtracted result is shown in Figure 62. Moving the detector to the left causes the peak to move to the right, as shown in Figure 61.

Comparing the peak heights of six positions along the central part of the array gives a peak height variance of 25%. To establish that the variance was due to differences in pixel sensitivity, a full field measurement was taken with no slit. Dividing the background subtracted slit image by the background subtracted full field image

causes the two peak heights shown in Figure 62 and Figure 61 to agree within 6%.

Unfortunately, problems have developed in advancing this technology from linear to two dimensional arrays. Although only one-dimensional arrays were proposed in this project, it was recognized that the eventual outcome should be a 2D array. The current technology for 2D CZT arrays do not lend themselves to the small pixel sizes and relatively low x-ray energies (compared to nuclear gamma imaging) required for mammography.

CID Detector

Because of the questions in development of the CZT technology we have investigated a second technology, Charge Injection Devices (CID), as well. Like the

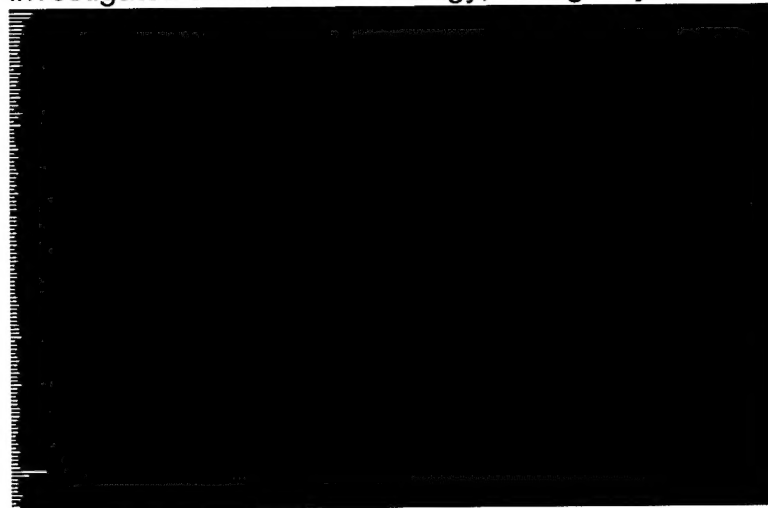


Figure 64. CID image of Lucite phantom shown in Figure 31.

more common CCD (Charge couple device) CID technology allows for rapid array imaging. Unlike the CCD, the CID is very radiation resistant. CID pixels can be read repeatedly and nondestructively, leading to very high dynamic range. CID well depths are also deeper than conventional CCDs, leading to a substantial reduction in blurring from high energy x-ray photons. The CID chips tested, which had

250x250 28 μm pixels, were too thin to have good x-ray quantum efficiency without phosphor. However, large area chip technology is already available. The measured DQE for the device was 23% at 20 keV. At that energy only 29% of the photons are expected to be absorbed in the 8 μm thick active region. Detector designs with thicker active areas will have larger DQEs. We will be working with the manufacturer, CIDTec, to study the application of their new x-ray dental imagers (with and without phosphor coatings) to mammography.

Conclusions

This is a high risk project with potentially very high gain. Any such project will have inevitable delays, frustrations and changes of direction. However, the delays and problems associated with this project have been fairly minor. Some manufacturing problems have occurred with both optics and detectors. These problems are being addressed by our studies of defect properties, and by changes being adopted in the manufacturing processes. Notwithstanding the problems, the optics tested have performed extremely well. A number of promising geometries are being studied: collimating optics with long and short focal lengths, with and without antiscatter optics, monolithic linear magnifying tapers, and monolithic focusing, demagnifying optics. The collimating optics have transmissions in excess of 30% at their design energies, with collection angles ranging from 8 to 12 degrees. Scatter rejection is very high from all the optics. The linear tapers resulted in nearly ideal contrast enhancements and simultaneously increase in MTF at all spatial frequencies. This will result in an improvement in resolution regardless the inherent spatial resolution of the detector. Just as important, if less spectacular, is the rapidly growing modeling capability. The modeling has lead to a real development of understanding of the nature of polycapillary defects, which is already leading to improvements in the manufacturing processes. Further, the increased confidence in the modeling allows future lens geometries to be effectively "tested" in simulation so that design parameters can be rapidly optimized.

Direct digital detector development is also promising. Two diverse detector technologies have been investigated. Both show considerable promise for providing simultaneous high resolution and high quantum efficiency. One dimensional "imaging" was demonstrated with the CZT linear array. The CZT detector has higher quantum efficiency without phosphor, but is more difficult to produce as a two-dimensional array with sufficiently low read-out noise and small enough pixels. However, this is largely a problem with the read-out electronics. As better electronics are becoming rapidly available, this technology becomes more attractive. The CID technology, while it would require some modification for phosphor free operation, is moving rapidly into the x-ray market, particularly in dental imaging. CID two dimensional array technology with small pixel sizes already exists. This is another promising new technology for mammography.

References

- ¹Shern, F., Digital Mammography and Related Technologies: A Perspective from the national Cancer Institute, Radiology, 183(3), p.629-630, 1992.
- ² M.A. Kumakhov, F.F. Komarov, "Multiple Reflection from Surface X-ray Optics," Physics Reports, **191**, (5): p. 289-350, 1990.
- ³ C.A. MacDonald, C.C. Abreu, S.S. Budkov, H. Chen, X. Fu, W.M. Gibson, Kardiawarman, A. Karnaukhov, V. Kovantsev, I. Ponomarev, B.K. Rath, J.B. Ullrich, M. Vartanian, Q.F. Xiao, "Quantitative Measurements of the Performance of Capillary X-ray Optics," Multilayer and Grazing Incidence X-ray/EUV Optics II, R.B. Hoover and A. Walker, eds., SPIE Proc. vol. 2011, 1993.
- ⁴ J.B Ullrich, V. Kovantsev, C.A. MacDonald, "Measurements of Polycapillary X-ray Optics," Jour. Appl. Phys., **74** (10), to be published, Nov. 15, 1993.
- ⁵ C.A. MacDonald, "Applications and Measurements of Polycapillary X-ray Optics," submitted, Journal of X-ray Science and Technology, Special Issue for the Proceedings of the Monochromatic X-ray Workshop, 11/93.
- ⁶ C. C. Abreu, D. G. Kruger, C. A. MacDonald, C. A. Mistretta, W. W. Peppler, Q. F. Xiao, Measurements of Capillary X-ray Optics with Potential for Use in Mammographic Imaging, accepted, Medical Physics.
- ⁷ A. G. Haus, in **Screen Film Mammography**, G.T. Barnes and G. Donald Frey, eds., Medical Physics Publishing, Madison, Wisconsin, 1991.
- ⁸ B.H. Hasegawa, The Physics of Medical X-ray Imaging, 2nd Ed., Medical Physics Publishing, Madison, Wisconsin, 1991.
- ⁹ Q.F. Xiao, I.Y. Ponomarev, A.I. Kolomitsev and J.C. Kimball, in R.B. Hoover, ed., **X-ray Detector Physics and Applications**, SPIE 1992.
- ¹⁰ B.L. Henke, E.M. Gullikson, and J.C. Davis, Atomic Data and Nuclear Data Tables, **54** (2), p. 181, 1993.
- ¹¹ Lei Wang, B.K. Rath, W.M. Gibson, J.C. Kimball, C.A. MacDonald, "Measurement and Analysis of Capillary Optic Performance for Hard X rays," Jour. Appl. Phys., September 15, 1996.

¹²Lei Wang and C.A. MacDonald, "Measurement of Capillary Optic Performance for Hard X rays," in R.B. Hoover and M.B. Williams, **X-ray and Ultraviolet Sensors and Applications**, SPIE vol. 2519, July 1995.

¹³Lei Wang and C.A. MacDonald, "Measurement and analysis of capillary optic performance for hard x-rays", **Hard X-ray/Gamma-Ray and Neutron Optics, Sensors, and Applications**, R.B. Hoover, and F.P. Doty, eds., SPIE Proceedings Vol. 2859.

¹⁴Bimal Rath, et al. In preparation.

¹⁵B.K. Rath, D.C. Aloisi, D.H. Bilderback, N. Gao, W.M. Gibson, F.A. Hofmann, B.E. Homan, C.J. Jezewski, I.L. Klotzko, J.M. Mitchell, S.M. Owens, J.B. Ullrich, Lei Wang, G.M. Wells, Q.F. Xiao, and C.A. MacDonald, Effects of intense x-ray radiation on polycapillary fiber performance, in R.B. Hoover and M.B. Williams, **X-Ray and Ultraviolet Sensors and Applications**, SPIE vol. 2519, July 1995.

¹⁶C.C. Abreu and C.A. MacDonald, *Physica Medica*, in press.

¹⁷D.G. Kruger, C.C. Abreu, W.W. Peppler, C.A. MacDonald, C.A. Mistretta, "Imaging Characteristics of X-ray Capillary Optics in Mammography," submitted, *Medical Physics*.